

Optical/NIR stellar absorption and emission-line indices from luminous infrared galaxies

Rogério Riffel^{1,1★†}, Alberto Rodríguez-Ardila^{2,3}, Michael S. Brotherton⁴,
Reynier Peletier⁵, Alexandre Vazdekis⁶, Rogemar A. Riffel⁷,
Lucimara Pires Martins⁸, Charles Bonatto¹, Natacha Zanon Dametto¹,
Luis Gabriel Dahmer-Hahn¹, Jessie Runnoe^{4,9}, Miriani G. Pastoriza¹,
Ana L. Chies-Santos¹ and Marina Trevisan¹

¹Departamento de Astronomia, Universidade Federal do Rio Grande do Sul, Av. Bento Gonçalves 9500, 91501-970 Porto Alegre, RS, Brazil

²Laboratório Nacional de Astrofísica/MCT - Rua dos Estados Unidos 154, Bairro das Nações. CEP 37504-364 Itajubá, MG, Brazil

³Divisão de Astrofísica, Instituto Nacional de Pesquisas Espaciais, 12227-010 São José dos Campos, SP, Brazil

⁴Department of Physics and Astronomy, University of Wyoming, Laramie, WY 82071, USA

⁵Kapteyn Astronomical Institute, University of Groningen, Postbus 800, NL-9700 AV, Groningen, the Netherlands

⁶Instituto de Astrofísica de Canarias, Vía Láctea, S/N, E-38205 La Laguna, Tenerife, Spain

⁷Departamento de Física, CCNE, Universidade Federal de Santa Maria (UFSM), 97105-900 Santa Maria, RS, Brazil

⁸NAT - Universidade Cruzeiro do Sul, Rua Galvão Bueno, 868, 01506-000 São Paulo, SP, Brazil

⁹Department of Astronomy, University of Michigan, 1085 S. University Ave., Ann Arbor, MI 48109, USA

Accepted 2019 April 11. Received 2019 March 11; in original form 2018 October 17

ABSTRACT

We analyse a set of optical-to-near-infrared long-slit nuclear spectra of 16 infrared-luminous spiral galaxies. All of the studied sources present H₂ emission, which reflects the star-forming nature of our sample, and they clearly display H I emission lines in the optical. Their continua contain many strong stellar absorption lines, with the most common features due to Ca I, Ca II, Fe I, Na I, Mg I, in addition to prominent absorption bands of TiO, VO, ZrO, CN, and CO. We report a homogeneous set of equivalent width (EW) measurements for 45 indices, from optical to NIR species for the 16 star-forming galaxies as well as for 19 early-type galaxies where we collected the data from the literature. This selected set of emission and absorption-feature measurements can be used to test predictions of the forthcoming generations of stellar population models. We find correlations among the different absorption features and propose here correlations between optical and NIR indices, as well as among different NIR indices, and compare them with model predictions. Although for the optical absorption features the models consistently agree with the observations, the NIR indices are much harder to interpret. For early-type spirals the measurements agree roughly with the models, while for star-forming objects they fail to predict the strengths of these indices.

Key words: stars: AGB and post-AGB – galaxies: bulges – galaxies: evolution – galaxies: stellar content.

1 INTRODUCTION

One challenge in modern astrophysics is to understand galaxy formation and evolution. Both processes are strongly related to the

star-formation history (SFH) of galaxies. Thus, the detailed study of the different stellar populations found in galaxies is one of the most promising ways to shed some light on their evolutionary histories. So far, stellar population studies have been concentrated mainly in the optical spectral range (e.g. Bica 1988; Worthey et al. 1994; Trager et al. 2000; Sánchez-Blázquez et al. 2006; González Delgado et al. 2015; Goddard et al. 2017; Martín-Navarro et al. 2018). In the near-infrared, (0.8–2.4 μ m, NIR) even with some work dating back to the 1980s (e.g. Rieke et al. 1980), stellar population studies have just started to become more common in the last two decades

* E-mail: riffel@ufrgs.br

† Visiting Astronomer at the Infrared Telescope Facility, which is operated by the University of Hawaii under Cooperative Agreement no. NCC 5-538 with the National Aeronautics and Space Administration, Office of Space Science, Planetary Astronomy Program.

Table 1. Near-infrared observation log and basic sample properties.

Source	α	δ	z	Obs. date	Exp. time (s)	Airmass	PA (deg)	Size (pc \times pc)	Activity	$\log(L_{\text{IR}}/L_{\odot})^*$	Morphology
NGC 23	00h09m53.4s	+25d55m26s	0.0157202	2010-10-07	29 \times 120	1.04	330	1348 \times 270	SFG ^a	11.05	SBa
NGC 520	01h24m35.1s	+03d47m33s	0.0080367	2010-10-04	16 \times 120	1.04	300	689 \times 138	SFG ^b	10.91	S0
NGC 660	01h43m02.4s	+13d38m42s	0.0029152	2010-10-06	24 \times 120	1.01	33	237 \times 50	Sy2/H II ^{b, c, d}	10.49	SBa pec
NGC 1055	02h41m45.2s	+00d26m35s	0.0036267	2010-10-04	16 \times 120	1.07	285	466 \times 62	LINER/H II ^{b, c, d}	10.09	Sbc
NGC 1134	02h53m41.3s	+13d00m51s	0.0129803	2010-10-04	16 \times 120	1.11	0	1113 \times 223	SFG ^e	10.83	S?
NGC 1204	03h04m39.9s	−12d20m29s	0.0154058	2010-10-07	16 \times 120	1.23	66	1321 \times 264	LINER ^f	10.88	S0/a
NGC 1222	03h08m56.7s	−02d57m19s	0.0082097	2010-10-06	24 \times 120	1.13	315	598 \times 141	SFG ^g	10.60	S0 pec
NGC 1266	03h16m00.7s	−02d25m38s	0.0077032	2010-10-07	18 \times 120	1.09	0	661 \times 132	LINER ^g	10.46	SB0 pec
UGC 2982	04h12m22.4s	+05d32m51s	0.0177955	2010-10-04	9 \times 120	1.11	295	1526 \times 305	SFG ^h	11.30	SB
NGC 1797	05h07m44.9s	−08d01m09s	0.0154111	2010-10-07	16 \times 120	1.23	66	1321 \times 264	SFG ^a	11.00	SBa
NGC 6814	19h42m40.6s	−10d19m25s	0.0056730	2010-10-07	16 \times 120	1.17	0	486 \times 97	Sy 1 ^g	10.25	SBbc
NGC 6835	19h54m32.9s	−12d34m03s	0.0057248	2010-10-06	22 \times 120	1.21	70	368 \times 98	SFG ⁱ	10.32	SBa
UGC 12150	22h41m12.2s	+34d14m57s	0.0214590	2010-10-04	15 \times 120	1.08	37	1656 \times 368	LINER/H II ^j	11.29	SB0/a
NGC 7465	23h02m01.0s	+15d57m53s	0.0066328	2010-10-06	12 \times 120	1.03	340	569 \times 114	LINER/Sy 2 ^k	10.10	SB0
NGC 7591	23h18m16.3s	+06d35m09s	0.0165841	2010-10-07	16 \times 120	1.03	0	1422 \times 284	LINER ^g	11.05	SBbc
NGC 7678	23h28m27.9s	+22d25m16s	0.0120136	2010-10-04	16 \times 120	1.01	90	927 \times 206	SFG ^l	10.77	SBc

Note. SFG: Star-forming galaxies (Starburst or H II galaxies). LINER/H II were assumed to be pure LINERs in the text. The galaxies are listed in order of right ascension, and the number of exposures refers to on-source integrations. The slit width is 0.8 arcsec.

^aBalzano (1983); ^bHo, Filippenko & Sargent (1997a); ^cHo et al. (1997b); ^dFilho et al. (2004); ^eCondon, Cotton & Broderick (2002); ^fSturm et al. (2006); ^gPereira-Santaella et al. (2010); ^hSchmitt et al. (2006); ⁱCoziol + 98; ^jVeilleux et al. (1995); ^kFerruit, Wilson & Mulchaey (2000); ^lGonçalves, Veron & Veron-Cetty (1998); ^mSanders et al. (2003).

(Origlia, Moorwood & Oliva 1993; Origlia et al. 1997; Riffel et al. 2007, 2008, 2009; Cesetti et al. 2009; Lyubenova et al. 2010; Chies-Santos et al. 2011a,b; Riffel et al. 2011c; Kotilainen et al. 2012; La Barbera et al. 2013; Martins et al. 2013b; Noël et al. 2013; Zibetti et al. 2013; Dametto et al. 2014; Riffel et al. 2015; Baldwin et al. 2017; Alton, Smith & Lucey 2018; Dahmer-Hahn et al. 2018, 2019; Francois et al. 2019; Dametto et al. 2019, for example). Models have shown that the NIR spectral features provide very important insights, particularly into the stellar populations dominated by cold stars (e.g. Maraston 2005; Riffel et al. 2007; Conroy & van Dokkum 2012; van Dokkum & Conroy 2012; Zibetti et al. 2013; Riffel et al. 2015; Röck 2015; Röck et al. 2016). For example, the stars in the thermally pulsing asymptotic giant branch (TP-AGB) phase may be responsible for nearly half of the luminosity in the *K* band for stellar populations with an age of ~ 1 Gyr (Maraston 1998, 2005; Salaris et al. 2014).

One common technique to study the unresolved stellar content of galaxies is the fitting of a combination of simple stellar populations (SSPs) to obtain the SFH. However, due to difficulties in theoretical treatment (Maraston 2005; Marigo et al. 2008; Noël et al. 2013) and the lack of complete empirical stellar libraries in the NIR (Lançon et al. 2001; Chen et al. 2014; Riffel et al. 2015; Villaume et al. 2017) the available SSP models produce discrepant results (e.g. Baldwin et al. 2017), thus making it very difficult to reliably analyse the SFH in the NIR.

On the other hand, the stellar content and chemical composition of the unresolved stellar populations of galaxies can also be obtained by the study of the observed absorption features present in their integrated spectra. So far, we still lack a comprehensive NIR data set to compare with model predictions, required to make improvements to the models and to lead to a better understanding of the role played by the cooler stellar populations in the integrated spectra of galaxies.

Among the best natural laboratories to study these kinds of stellar content are *infrared galaxies*, sources that emit more energy in the infrared ($\sim 5\text{--}500\ \mu\text{m}$) than at all the other wavelengths combined (Sanders & Mirabel 1996; Sanders et al. 2003). The relevance of

studying these galaxies lies particularly in the fact that they are implicated in a variety of interesting astrophysical phenomena, including the formation of quasars and elliptical galaxies (e.g. Genzel et al. 2001; Veilleux 2006; Wang et al. 2006). When studying luminous infrared galaxies in the Local Universe, it is possible to obtain high-angular-resolution observations of these objects, thus allowing the investigation of their very central regions. Comparison of such objects with those at higher redshifts may help to understand the SFH over cosmic times.

With the above in mind, we obtained optical and NIR spectra of a subsample of galaxies selected from the *IRAS* Revised Bright Galaxy Sample present in the Local Universe. These galaxies are believed to be experiencing massive star formation, making them suitable for studying their most important spectral features that can be used as proxies to test and constrain stellar-population models. As part of a series of papers aimed at studying the stellar population and gas emission features, here we provide measurements for the most conspicuous emission and absorption features, and present new correlations between absorption features. The outline of the paper is as follows: in Section 2 we describe the observations and data reduction. The results are presented and discussed in Section 3. Final remarks are made in Section 5.

2 OBSERVATIONS AND DATA REDUCTION

Our sample is composed of 16 Local Universe ($v_r \lesssim 6400\ \text{km s}^{-1}$) galaxies that are very bright in the infrared (see Table 1). They were selected from the *IRAS* Revised Bright Galaxy Sample, which is regarded as a statistically complete sample of 629 galaxies, with $60\ \mu\text{m}$ flux density $\gtrsim 5.24\ \text{Jy}$. Galaxies chosen for this study were those with $\log(L_{\text{IR}}/L_{\odot}) \gtrsim 10.10$, accessible from the Infrared Telescope Facility (IRTF) and the Wyoming Infrared Observatory (WIRO, see below), and bright enough to reach an S/N ~ 100 in the *K* band within a reasonable on-source integration time.

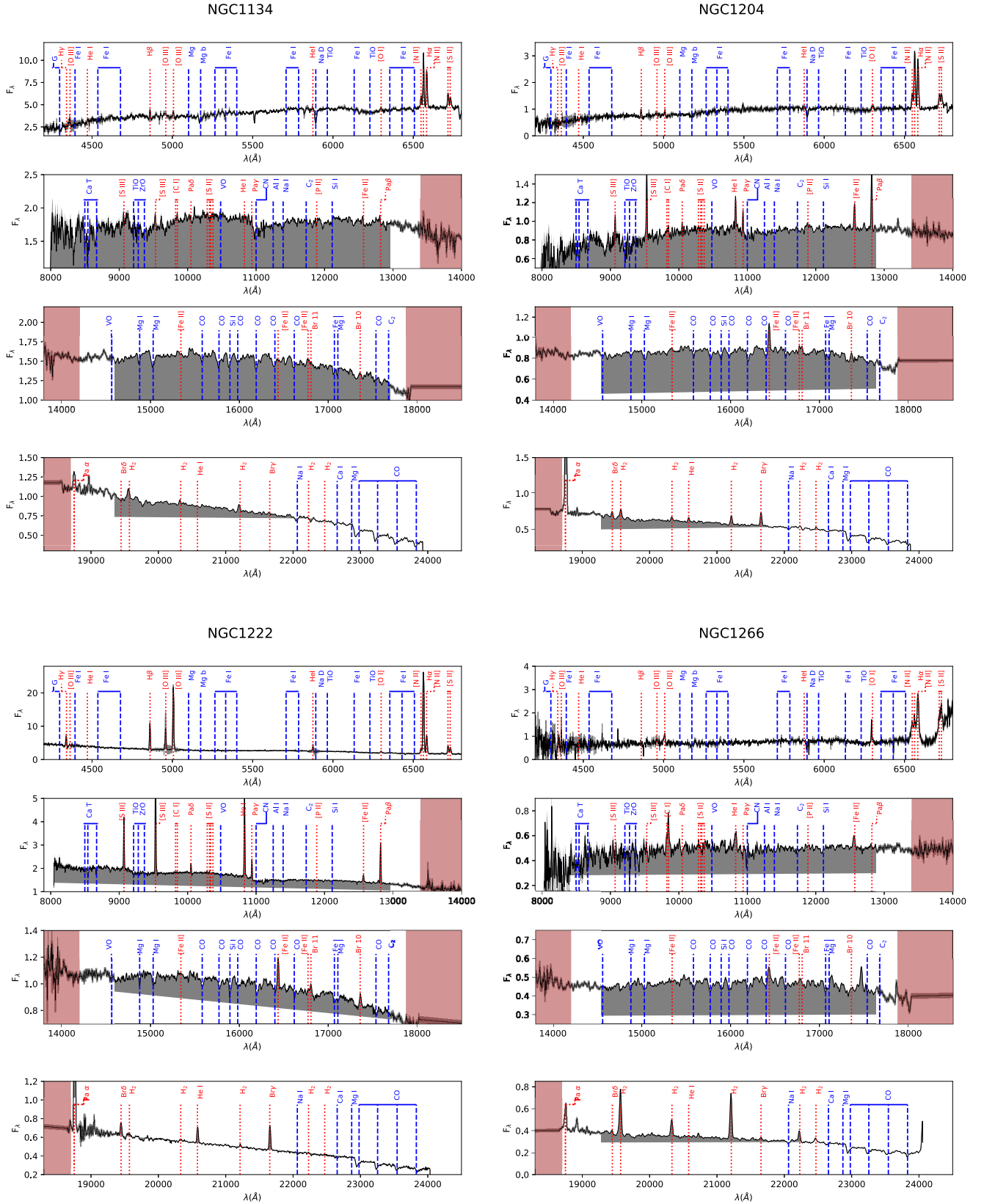


Figure 1. Final reduced and redshift-corrected spectra for NGC 1134, NGC 1204, NGC 1222, and NGC 1266. For each galaxy we show from top to bottom the optical, $z + J$, H , and K bands, respectively. The flux is in units of $10^{-15} \text{ erg cm}^{-2} \text{ s}^{-1}$. The shaded grey area represents the uncertainties and the brown area indicates the poor transmission regions between different bands. The remaining spectra are shown in online material.

Table 2. Optical observation log. The slit was oriented north–south.

Source	Obs. date	Exp. time (s)	Airmass	Size (pc × pc)
NGC 23	2010-10-04	600	1.20	2359 × 1348
NGC 520	2010-10-03	600	1.28	4307 × 689
NGC 660	2010-10-04	600	1.18	437 × 250
NGC 1055	2010-10-04	600	1.36	544 × 311
NGC 1134	2010-10-04	600	1.14	12 243 × 1113
NGC 1204	2010-10-04	600	1.68	2312 × 1321
NGC 1222	2010-10-03	600	1.42	3344 × 704
NGC 1266	2010-10-03	600	1.39	6440 × 661
UGC 2982	2010-10-04	600	1.27	2670 × 1526
NGC 1797	2010-10-02	600	1.56	11 893 × 1321
UGC 12150	2010-10-03	600	1.03	18 401 × 1840
NGC 7465	2010-10-03	600	1.12	3270 × 569
NGC 7591	2010-10-03	600	1.21	13 154 × 1422
NGC 7678	2010-10-04	600	1.18	1803 × 1030

Note. The slit width is 4 arcsec.

2.1 Near-infrared data

Cross-dispersed NIR spectra in the range 0.8–2.4 μm were obtained on 2010 October 4, 6, and 7 with the SpeX spectrograph (Rayner et al. 2003) attached to the NASA 3 m IRTF telescope at the Mauna Kea observing site. The detector is a 1024×1024 ALADDIN 3 InSb array with a spatial scale of 0.15 arcsec pixel^{−1}. A 0.8 arcsec × 15 arcsec slit was used during the observations, giving a spectral resolution of $R \sim 1000$ (or $\sigma = 127 \text{ km s}^{-1}$). Both the arc lamp spectra and the night-sky spectra are consistent with this value (Riffel et al. 2013a). The observations were done by nodding in an Object-Sky-Object pattern with typical individual integration times of 120 s and total on-source integration times between 18 and 58 min. During the observations, A0 V stars were observed near each target to provide telluric standards at similar air masses. These stars were also used to flux calibrate the galaxy spectra using blackbody functions to calibrate the observed spectra of the standard stars. The seeing varied between 0.4 and 0.7 arcsec over the different nights and there were no obvious clouds.

We reduced the NIR observations following the standard data reduction procedures given by Riffel, Rodríguez-Ardila & Pastoriza (2006) and Riffel et al. (2013b). In short, spectral extraction and wavelength calibration were performed using SPEXTOOL, software developed and provided by the SpeX team for the IRTF community (Cushing, Vacca & Rayner 2004). The area of the integrated region is listed in Table 1. Each extraction was centred at the peak of the continuum-light distribution for every object of the sample. No effort was made to extract spectra at positions different from the nuclear region, even though some objects show evidence of extended emission, as this goes beyond the scope of this analysis. Telluric absorption correction and flux calibration were applied to the individual 1D spectra by means of the IDL routine *xtellcor* (Vacca, Cushing & Rayner 2003).

2.2 Optical data

For completeness, the same sample was also observed in the optical range on nearly the same dates as the NIR data were collected with the WIRO long-slit spectrograph. The instrument is attached to the University of Wyoming’s 2.3-m telescope, located on Jelm Mountain at WIRO. The Cassegrain-mounted instrument uses a Marconi 2k × 2k CCD detector. During our observations we used a

900 l/mm grating in first order to obtain spectra from approximately 4000–7000 Å calibrated with a CuAr comparison lamp. Given our 4-arcsec slit oriented north–south, the resolution was $R \sim 1200$. Due to the relatively large spatial extent of these low-redshift objects, we offset the telescope pointing by 2 arcmin to obtain sky spectra uncontaminated by galaxy light. The seeing varied between 1 and 2 arcsec during the nights of observation. We reduced the spectra using standard techniques in IRAF.¹ Table 1 shows the observation log along with extraction apertures. The 1D wavelength and flux-calibrated spectra were then corrected for redshift, determined from the average z measured from the position of [S III] 0.953 μm , Pa δ , He I 1.083 μm , Pa β , and Br γ .

Examples of the final reduced spectra, from optical to NIR (~ 0.4 –2.4 μm) are presented in Fig. 1, for the remaining galaxies see Appendix A. For each galaxy we show the optical, $z + J$, H , and K bands, from top to bottom, respectively. It is worth mentioning that the optical and NIR data do not share the same apertures, and the slit was not generally oriented at the same position angles. However, since we are interested in the nuclear region, the different slit orientations should not introduce large discrepancies in the measurements. The ordinate axis represents the monochromatic flux in units of $10^{-15} \text{ erg cm}^{-2} \text{ s}^{-1} \text{ Å}^{-1}$. The position of the most common and expected emission and absorption lines are indicated as dotted (red) and dashed (blue) lines, respectively.

3 RESULTS

3.1 Emission-line spectra

A visual inspection of the data reveals a wide diversity of emission-line strengths and species. The most common emission features detected are: H β , [O III] 4959, 5007 Å, [N II] 6548, 6583 Å, H α , [S II] 6716, 6730 Å, [S III] 9531 Å, Pa δ , [C I] 9824, 9850 Å, Pa β , He I 10830 Å, [P II] 11886 Å, [Fe II] 12570, 16436 Å, Pa α H $_2$ 19570 Å, H $_2$ 21218 Å, and Br γ .

Emission-line fluxes for each object of the sample were measured by fitting a Gaussian function to the observed profile and then integrating the flux under the curve. The LINER software (Pogge & Owen 1993) was used for this purpose. No attempt to correct for stellar absorption was made before measuring the emission lines. This was done because NIR models with adequate spectral resolution (to allow the measurements of the weaker emission lines) are not available for the younger ages. Martins et al. (2013a) have shown that the underlying stellar population has only a strong effect on the hydrogen recombination emission lines, with the largest differences in fluxes being about 25 per cent. This value is within the largest uncertainties on the fluxes values too. For completeness, we have not subtracted the stellar features from the optical range too.

The results, including 3σ uncertainties, are listed in Tables 3 and 4. For most of our targets, these measurements are made public for the first time. In addition, we computed the extinction coefficient, C_{ext} , for the NIR using the intrinsic value of 5.88 for the flux ratio of Pa β /Br γ (Hummer & Storey 1987, using case B). The Cardelli, Clayton & Mathis (1989) extinction law was used, and the values obtained for the coefficients are listed in Tables 3 and 4.

¹IRAF is distributed by the National Optical Astronomy Observatories, which are operated by the Association of Universities for Research in Astronomy, Inc., under cooperative agreement with the National Science Foundation.

Table 3. Emission-line fluxes in units of $1 \times 10^{-15} \text{ erg cm}^{-2} \text{ s}^{-1}$.

Line	Ion	NGC 23	NGC 520	NGC 660	NGC 1055	NGC 1134	NGC 1204	NGC 1222	NGC 1266
	C_{ext}	–	–	3.42 ± 0.13	–	–	2.95 ± 0.14	1.06 ± 0.05	6.74 ± 0.73
4861	H β	20.40 ± 1.16	–	0.86 ± 0.26	–	6.06 ± 0.37	0.30 ± 0.06	49.30 ± 0.65	–
4959	[O III]	30.70 ± 3.13	–	3.37 ± 0.41	–	8.25 ± 0.72	1.69 ± 0.48	47.30 ± 0.75	–
5007	[O III]	10.50 ± 3.13	2.16 ± 0.30	1.15 ± 0.41	–	2.81 ± 0.72	0.58 ± 0.48	140.00 ± 0.75	4.27 ± 0.64
6548	[N II]	108.00 ± 3.26	1.60 ± 0.31	6.25 ± 0.53	1.41 ± 0.32	12.90 ± 1.41	5.75 ± 0.43	14.20 ± 0.40	14.30 ± 1.07
6563	H α	83.80 ± 3.89	8.68 ± 0.44	17.20 ± 0.46	4.97 ± 0.34	40.50 ± 0.95	20.50 ± 0.42	222.00 ± 0.43	11.40 ± 0.76
6583	[N II]	27.90 ± 3.89	6.96 ± 0.49	18.60 ± 0.48	4.56 ± 0.39	38.30 ± 1.21	18.60 ± 0.42	49.70 ± 0.45	30.60 ± 0.87
6716	[S II]	46.50 ± 1.92	3.29 ± 0.46	5.15 ± 0.48	1.25 ± 0.29	14.60 ± 1.23	5.76 ± 1.23	20.70 ± 0.48	18.70 ± 1.16
6730	[S II]	34.70 ± 1.92	3.07 ± 0.55	4.88 ± 0.61	1.31 ± 0.44	12.90 ± 1.50	5.69 ± 1.23	19.90 ± 0.57	21.10 ± 1.16
9069	[S III]	14.80 ± 3.96	–	–	–	–	10.30 ± 1.40	32.80 ± 1.59	–
9531	[S III]	15.70 ± 3.96	–	23.90 ± 0.94	–	–	11.90 ± 0.54	72.60 ± 1.49	–
9824	[C I]	1.57 ± 0.60	–	2.10 ± 0.27	–	–	1.15 ± 0.30	1.55 ± 0.49	–
9850	[C I]	5.15 ± 0.60	–	2.53 ± 0.27	–	–	1.88 ± 0.30	0.97 ± 0.49	9.21 ± 1.06
10049	Pa δ	–	–	2.55 ± 0.22	–	–	1.03 ± 0.08	4.05 ± 0.31	–
10122	He II	–	–	2.78 ± 0.22	–	–	1.34 ± 0.08	–	–
10830	He I	22.30 ± 2.60	–	13.30 ± 0.41	–	–	9.24 ± 0.56	53.80 ± 0.77	6.26 ± 0.83
10938	Pa γ	5.65 ± 1.58	–	8.57 ± 0.31	–	–	2.78 ± 0.27	12.90 ± 0.76	–
11470	[P II]	–	–	1.82 ± 1.09	–	–	1.17 ± 0.27	–	–
11886	[P II]	–	–	3.68 ± 1.09	–	–	1.70 ± 0.19	–	–
12567	[Fe II]	10.50 ± 0.87	–	13.90 ± 0.65	–	–	5.16 ± 0.20	6.32 ± 0.43	3.19 ± 0.51
12820	Pa β	–	–	29.00 ± 0.60	–	–	12.10 ± 0.20	28.20 ± 0.37	0.75 ± 0.08
12950	[Fe II]	–	–	1.21 ± 0.15	–	–	1.35 ± 0.25	–	–
13209	[Fe II]	–	–	6.60 ± 0.24	–	–	4.49 ± 0.39	–	–
15342	[Fe II]	–	–	–	–	–	1.52 ± 0.36	–	–
16436	[Fe II]	14.20 ± 3.46	3.87 ± 0.14	15.70 ± 0.90	–	–	6.51 ± 0.36	4.65 ± 0.18	2.90 ± 0.38
16773	[Fe II]+Br I 1	31.50 ± 1.34	–	–	–	–	2.65 ± 0.50	–	–
17360	Br I 0	–	–	–	–	–	1.60 ± 0.13	–	–
18750	Pa α	–	35.40 ± 0.30	60.20 ± 1.64	–	–	61.10 ± 0.33	69.30 ± 0.57	8.03 ± 0.34
19446	Br δ	–	2.07 ± 0.28	5.67 ± 0.53	–	–	1.80 ± 0.34	3.78 ± 0.20	–
19570	H ₂	20.20 ± 4.60	2.41 ± 0.39	8.87 ± 0.80	1.24 ± 0.3	–	4.17 ± 0.51	1.95 ± 0.34	15.10 ± 0.47
20332	H ₂	4.94 ± 0.57	1.13 ± 0.10	3.67 ± 0.56	–	1.14 ± 0.3	1.81 ± 0.34	0.95 ± 0.14	5.10 ± 0.44
20580	H ₂	–	2.47 ± 0.09	5.32 ± 0.64	–	–	1.47 ± 0.27	4.68 ± 0.14	–
21218	H ₂	10.00 ± 1.26	2.40 ± 0.18	6.91 ± 0.72	0.6 ± 0.08	2.37 ± 0.4	3.61 ± 0.25	0.84 ± 0.12	13.70 ± 0.25
21654	Br γ	–	6.67 ± 0.19	16.60 ± 0.71	–	–	5.88 ± 0.27	6.98 ± 0.07	1.40 ± 0.33
22230	H ₂	4.53 ± 2.97	0.67 ± 0.19	2.01 ± 1.20	–	–	0.87 ± 0.09	0.49 ± 0.19	3.26 ± 0.12
22470	H ₂	1.47 ± 0.37	0.83 ± 0.12	1.18 ± 0.12	–	–	0.72 ± 0.10	0.29 ± 0.04	1.51 ± 0.14

3.2 The continuum spectra

The main goal of this section is to characterize the continuum emission observed in our sample and compare it to other data in the literature. To help in the visual inspection² of the individual spectra, we normalized the continuum emission to unity in two regions free from emission/absorption features taken from Riffel et al. (2011b). The NIR spectra were normalized at 20925 Å and then sorted according to their continuum shapes. For a proper comparison with the optical portion of the spectrum, we normalized the optical spectra at 5300 Å and plotted them in the same order as the NIR spectra (Figs 4 and 5).

A first-order inspection of Fig. 4 allows us to infer that, contrary to what happens in Seyfert galaxies (Riffel et al. 2006), there seems to be no correlation between activity type (LINERs or SFGs) and continuum shape. In fact, these very bright infrared galaxies present a continuum shape very similar to what is found in fainter H II sources and normal galaxies, as reported by Martins et al. (2013a), which may indicate that the LINER spectrum of these galaxies is powered by starburst instead of a low-luminosity AGN. In addition, the continua of all the optical spectra look very similar.

²Emission lines and equivalent widths of the absorption features were measured on the spectra previous to normalization.

A large diversity of atomic absorption lines and molecular bands is also apparent in the spectra. These features are seen from the very blue optical end to the red end of the observed NIR spectral region. The most common atomic absorption features are due to Ca I, Ca II, Fe I, Si I, Na I, and Mg I, besides the prominent absorption bands of CH, MgH, TiO, VO, ZrO, and CO. These features are identified in Fig. 1. It is clear in these figures that some of the most important features predicted for intermediate-age stellar populations, which are expected to be enhanced in the RGB and TP-AGB stellar phases (Maraston 2005; Riffel et al. 2007, 2015), are detected in the spectra. Among these features are the ZrO/CN/VO at 9350 Å, the 10 560 Å VO, 1.1 μm CN, and 1.6 and 2.3 μm CO bands.

3.2.1 Towards a homogeneous NIR index definition

The equivalent widths (EWs) of these features offer coarse but robust information about the stellar content of a galaxy spectrum, and therefore they can be used as powerful diagnostics of the stellar content of galaxies. Contrary to the optical range, where there exist indices defined in a homogeneous way by the Lick group (see Worthey et al. 1994, and references), in the NIR there is no such homogeneous set of definitions covering the full NIR wavelength range, and authors tend to use their own definitions (e.g. Riffel

Table 4. Continuation of Table 3.

Line	Ion	UGC2982	NGC 1797	NGC 6814*	NGC 6835	UGC12150	NGC 7465	NGC 7591	NGC 7678
	C_{ext}	–	2.68 ± 0.08	0.00	4.87 ± 0.19	2.16 ± 0.17	2.35 ± 0.93	2.53 ± 0.07	1.39 ± 0.23
4861	H β	0.49 ± 0.15	13.10 ± 0.71	–	–	–	21.80 ± 1.05	–	9.45 ± 0.42
4959	[O III]	0.35 ± 0.16	–	–	–	–	31.40 ± 2.27	–	–
5007	[O III]	0.76 ± 0.29	3.11 ± 0.44	–	–	–	56.00 ± 1.85	–	2.83 ± 0.54
6548	[N II]	1.64 ± 0.39	11.20 ± 0.59	–	–	–	29.50 ± 1.03	8.15 ± 1.36	7.88 ± 0.82
6563	H α	13.90 ± 0.40	88.70 ± 0.74	–	–	–	122.00 ± 0.89	21.10 ± 1.00	53.40 ± 1.00
6583	[N II]	5.62 ± 0.39	46.40 ± 0.76	–	–	–	71.10 ± 0.98	18.60 ± 1.04	27.60 ± 1.00
6716	[S II]	2.77 ± 0.45	10.80 ± 0.41	–	–	–	39.70 ± 1.17	4.87 ± 1.94	9.23 ± 0.97
6730	[S II]	2.66 ± 0.75	10.30 ± 0.46	–	–	–	34.10 ± 1.22	3.46 ± 1.94	10.30 ± 1.37
9069	[S III]	–	5.80 ± 0.59	23.70 ± 0.49	–	5.16 ± 0.27	18.00 ± 1.43	–	6.59 ± 0.64
9531	[S III]	–	12.10 ± 0.59	55.50 ± 0.58	–	5.22 ± 0.20	38.20 ± 0.78	10.00 ± 0.32	15.60 ± 0.64
9824	[C I]	–	1.71 ± 0.16	–	–	–	2.41 ± 0.76	0.98 ± 0.15	0.82 ± 0.09
9850	[C I]	–	1.67 ± 0.16	–	–	2.49 ± 0.17	3.32 ± 0.76	2.58 ± 0.15	1.74 ± 0.09
10049	Pa δ	–	–	–	–	–	–	3.85 ± 0.44	–
10122	He II	–	–	–	–	–	–	3.28 ± 0.23	–
10830	He I	–	7.72 ± 1.08	–	–	8.40 ± 1.23	25.60 ± 1.52	8.41 ± 0.88	9.47 ± 0.77
10938	Pa γ	–	3.98 ± 1.08	–	–	2.57 ± 0.57	8.07 ± 1.20	3.02 ± 0.47	4.08 ± 0.55
11470	[P II]	–	1.30 ± 0.37	–	–	1.17 ± 0.14	–	2.50 ± 0.87	–
11886	[P II]	–	1.80 ± 0.37	3.83 ± 1.08	–	1.46 ± 0.14	–	4.98 ± 0.87	–
12567	[Fe II]	–	5.04 ± 0.25	4.64 ± 0.52	2.06 ± 0.23	4.73 ± 0.33	11.80 ± 0.66	6.80 ± 0.21	3.28 ± 0.49
12820	Pa β	–	12.10 ± 0.26	3.53 ± 0.57	4.86 ± 0.19	7.86 ± 0.30	9.57 ± 2.61	9.74 ± 0.21	9.20 ± 0.51
12950	[Fe II]	–	1.18 ± 0.42	–	–	–	–	–	–
13209	[Fe II]	–	2.94 ± 0.42	–	–	–	5.60 ± 0.34	–	–
15342	[Fe II]	–	–	–	–	–	–	–	–
16436	[Fe II]	–	4.65 ± 0.47	5.53 ± 0.48	3.24 ± 0.08	3.56 ± 0.18	9.20 ± 0.28	6.05 ± 0.60	3.09 ± 0.21
16773	[Fe II]+Br11	–	–	–	–	–	–	–	–
17360	Br10	–	–	–	–	–	–	–	–
18750	Pa α	4.70 ± 0.18	60.40 ± 0.46	82.50 ± 3.49	32.60 ± 0.29	34.30 ± 0.17	31.60 ± 3.36	36.70 ± 0.67	23.30 ± 0.32
19446	Br δ	–	2.12 ± 0.39	–	2.36 ± 0.22	–	–	–	1.05 ± 0.10
19570	H $_2$	1.79 ± 0.49	4.10 ± 0.52	3.36 ± 0.54	3.33 ± 0.44	5.25 ± 0.05	4.33 ± 0.16	8.17 ± 0.26	1.45 ± 0.10
20332	H $_2$	0.61 ± 0.08	1.48 ± 0.30	1.25 ± 0.20	0.86 ± 0.05	1.65 ± 0.07	2.36 ± 0.39	2.46 ± 0.20	2.03 ± 0.20
20580	H $_2$	–	1.40 ± 0.26	–	1.98 ± 0.05	–	1.33 ± 0.34	1.53 ± 0.18	1.24 ± 0.20
21218	H $_2$	0.60 ± 0.02	3.21 ± 0.28	2.14 ± 0.20	1.34 ± 0.21	4.00 ± 0.13	3.92 ± 0.27	4.80 ± 0.36	0.88 ± 0.14
21654	Br γ	0.80 ± 0.04	5.33 ± 0.09	0.52 ± 0.32	4.66 ± 0.25	2.88 ± 0.13	3.75 ± 0.69	4.07 ± 0.05	2.56 ± 0.15
22230	H $_2$	–	1.20 ± 0.17	1.05 ± 0.23	0.65 ± 0.18	1.70 ± 0.85	1.71 ± 0.10	2.25 ± 0.25	0.71 ± 0.03
22470	H $_2$	–	1.18 ± 0.16	0.61 ± 0.13	–	0.55 ± 0.12	0.49 ± 0.06	1.30 ± 0.26	0.32 ± 0.14

et al. 2007, 2008; Silva, Kuntschner & Lyubenova 2008; Cesetti et al. 2009; Mármol-Queraltó et al. 2009; Riffel et al. 2011a, 2015; Kotilainen et al. 2012; Röck et al. 2017), and therefore it is very difficult to compare results from different investigations.

With this in mind, here we create a set of definitions for absorption features found in the NIR. We used two SSPs from the IRTF-based EMILES models (Röck 2015; Röck et al. 2016; Vazdekis et al. 2016), with 1.0 and 10 Gyr, solar metallicity, calculated with the PADOVA evolutionary tracks and with $\sigma = 228 \text{ km s}^{-1}$. We added up their light fractions (normalized to unity at $\lambda = 12230 \text{ \AA}$) as follows:

$$F_{\text{comb}} = 0.5 \frac{F_{\lambda}^{1 \text{ Gyr}}}{F_{\lambda=12230}^{1 \text{ Gyr}}} + 0.5 \frac{F_{\lambda}^{10 \text{ Gyr}}}{F_{\lambda=12230}^{10 \text{ Gyr}}}.$$

To this resulting spectrum we added Gaussians to model emission-lines profiles. These lines are located at the wavelengths of the most common emission lines detected in galaxies in this spectral region (see Section 3.1) with full width at half-maximums (FWHMs) characteristic of galaxies observed with SpeX with the configuration used here ($25 \text{ \AA} \lesssim \text{FWHM} \lesssim 40 \text{ \AA}$) with arbitrary flux values. We employed the ELPROFILE routine of the IFSCUBE package³ (Ruschel-

Dutra, in preparation). Using this simulated spectrum we defined the line limits and continuum band passes as illustrated in Fig. 3 and listed in Table 5.

We have measured the EWs for the most prominent absorption features using an updated PYTHON version of the PACCE code (Riffel & Borges Vale 2011). In this code version, the EW uncertainties are assumed to be the standard deviation of 1000 EWs measurements of simulated spectra created by perturbing each flux point by its uncertainty through a Monte Carlo approach. The line definitions used are listed in Table 5, and the measured values are in Tables 6 and 7. In order to have a sample of early-type galaxies (ETGs) to compare our results with, we have collected NIR spectra from the literature and measured the EW of the absorption features with the same definitions used for our sample. Tables B1 and B2 present the measurements for the sample of galaxies presented in Baldwin et al. (2017). For four of the galaxies we were able to find Sloan Digital Sky Survey data used to measure the optical EW, while for the remaining objects we collected the values of Fe5015, Mg $_b$ and Fe5270 from McDermid et al. (2015). We also measured the values from the spectra presented by Dahmer-Hahn et al. (2018), which values are listed in Table B3.

³Available at: <https://bitbucket.org/danielrld6/ifscube.git>.

Table 5. Line limits and continuum bandpasses.

Centre (Å)	Main absorber	Index name	Line limits (Å)	Blue continuum (Å)	Red continuum (Å)	Reference
4228.5	Ca I	Ca4227	4222.250–4234.750	4211.000–4219.750	4241.000–4251.000	Worthey et al. (1994)
4298.875	CH (G band)	G4300	4281.375–4316.375	4266.375–4282.625	4318.875–4335.125	Worthey et al. (1994)
4394.75	Fe I	Fe4383	4369.125–4420.375	4359.125–4370.375	4442.875–4455.375	Worthey et al. (1994)
4463.375	Ca I	Ca4455	4452.125–4474.625	4445.875–4454.625	4477.125–4492.125	Worthey et al. (1994)
4536.75	Fe I	Fe4531	4514.250–4559.250	4504.250–4514.250	4560.500–4579.250	Worthey et al. (1994)
4677.125	C ₂	Fe4668	4634.000–4720.250	4611.500–4630.250	4742.750–4756.500	Worthey et al. (1994)
5015.875	Fe I	Fe5015	4977.750–5054.000	4946.500–4977.750	5054.000–5065.250	Worthey et al. (1994)
5101.625	MgH	Mg1	5069.125–5134.125	4895.125–4957.625	5301.125–5366.125	Worthey et al. (1994)
5175.375	MgH	Mg2	5154.125–5196.625	4895.125–4957.625	5301.125–5366.125	Worthey et al. (1994)
5176.375	Mg b	Mgb	5160.125–5192.625	5142.625–5161.375	5191.375–5206.375	Worthey et al. (1994)
5265.65	Fe I	Fe5270	5245.650–5285.650	5233.150–5248.150	5285.650–5318.150	Worthey et al. (1994)
5332.125	Fe I	Fe5335	5312.125–5352.125	5304.625–5315.875	5353.375–5363.375	Worthey et al. (1994)
5401.25	Fe I	Fe5406	5387.500–5415.000	5376.250–5387.500	5415.000–5425.000	Worthey et al. (1994)
5708.5	Fe I	Fe5709	5696.625–5720.375	5672.875–5696.625	5722.875–5736.625	Worthey et al. (1994)
5786.625	Fe I	Fe5782	5776.625–5796.625	5765.375–5775.375	5797.875–5811.625	Worthey et al. (1994)
5893.125	Na I	NaD	5876.875–5909.375	5860.625–5875.625	5922.125–5948.125	Worthey et al. (1994)
5965.375	TiO	TiO1	5936.625–5994.125	5816.625–5849.125	6038.625–6103.625	Worthey et al. (1994)
6230.875	TiO	TiO2	6189.625–6272.125	6066.625–6141.625	6372.625–6415.125	Worthey et al. (1994)
8498.0	Ca II	CaT1	8476.000–8520.000	8110.000–8165.000	8786.000–8844.000	Bica & Alloin (1987) (†)
8542.0	Ca II	CaT2	8520.000–8564.000	8110.000–8165.000	8786.000–8844.000	Bica & Alloin (1987) (†)
8670.0	Ca II	CaT3	8640.000–8700.000	8110.000–8165.000	8786.000–8844.000	Bica & Alloin (1987) (†)
9320.0	ZrO/TiO/CN	ZrO	9170.000–9470.000	8900.000–8960.000	9585.000–9615.000	New Definition (α)
10 560.0	VO	VO	10 470.000–10 650.000	10 430.000–10 465.000	10 660.000–10 700.000	New Definition (α)
11 000.0	CN	CN11	10 910.000–11 090.000	10 705.000–10 730.000	11 310.000–11 345.000	New Definition (β)
11 390.0	Na I	NaI1.14	11 350.000–11 430.000	11 310.000–11 345.000	11 450.000–11 515.000	New Definition (β)
11 605.0	Fe I	FeI1.16	11 580.000–11 630.000	11 450.000–11 515.000	11 650.000–11 690.000	Roeck (2015)
12 430.0	Mg I	MgI1.24	12 405.000–12 455.000	12 335.000–12 365.000	12 465.000–12 490.000	Roeck (2015)
12 944.0	Mn I	MnI1.29	12 893.000–12 995.000	12 858.000–12 878.000	13 026.000–13 068.000	New Definition
13 132.5	Al I	AlI1.31	13 095.000–13 170.000	13 000.000–13 070.000	13 175.000–13 215.000	Roeck (2015)
14 875.0	Mg I	MgI1.48	14 850.000–14 900.000	14 750.000–14 800.000	14 910.000–14 950.000	New Definition
15 032.5	Mg I	MgI1.50	14 995.000–15 070.000	14 910.000–14 950.000	15 150.000–15 200.000	New Definition
15 587.5	CO+Mg I	CO1.5a	15 555.000–15 620.000	15 470.000–15 500.000	15 700.000–15 730.000	New Definition (ϵ)
15 780.0	CO+Mg I	CO1.5b	15 750.000–15 810.000	15 700.000–15 730.000	16 095.000–16 145.000	New Definition (ϵ)
15 830.0	Fe I	FeI1.58	15 810.000–15 850.000	15 700.000–15 730.000	16 090.000–16 140.000	New Definition
15 890.0	Si I+Mg I	SiI1.58	15 850.000–15 930.000	15 700.000–15 730.000	16 090.000–16 140.000	New Definition
15 985.0	CO+Si I	CO1.5c	15 950.000–16 020.000	15 700.000–15 730.000	16 090.000–16 140.000	New Definition (ϵ)
16 215.0	CO+Si I+Ca I	CO1.6a	16 145.000–16 285.000	16 090.000–16 140.000	16 290.000–16 340.000	New Definition (ϵ)
17 064.0	CO+Fe I	CO1.6b	17 035.000–17 093.000	16 970.000–17 025.000	17 140.000–17 200.000	New Definition (ϵ)
17 111.5	Mg I	MgI1.7	17 093.000–17 130.000	16 970.000–17 025.000	17 140.000–17 200.000	Roeck (2015)
22 073.5	Na I	NaI2.20	22 040.000–22 107.000	21 910.000–21 966.000	22 125.000–22 160.000	Frogel et al. (2001)
22 634.5	Ca I	CaI2.26	22 577.000–22 692.000	22 530.000–22 560.000	22 700.000–22 720.000	Frogel et al. (2001) (γ)
22 820.0	Mg I	MgI2.28	22 795.000–22 845.000	22 700.000–22 720.000	22 850.000–22 865.000	New Definition (δ)
23 015.0	CO	CO2.2	22 870.000–23 160.000	22 700.000–22 790.000	23 655.000–23 680.000	New Definition (ϵ)
23 290.0	CO	CO2.3a	23 160.000–23 420.000	22 700.000–22 790.000	23 655.000–23 680.000	New Definition (ϵ)
23 535.0	CO	CO2.3b	23 420.000–23 650.000	22 700.000–22 790.000	23 655.000–23 680.000	New Definition (ϵ)

Note. The optical indices are those of the LICK observatory (Worthey et al. 1994, and references). The CaT indices are those of Bica & Alloin (1987) with a change in the blue continuum band passes in order to fit in our spectral region; α Based on Riffel et al. (2015) with small changes on the line limits; β New continuum limits with central bandpasses from Roeck (2015); ϵ adapted from Riffel et al. (2007) with fixed continuum band passes, with better identifications of the main absorbers as well as better constraints of the line limits; γ We made a small change on the blue continuum band pass to remove possible H₂ emission lines.; δ Adapted from Silva et al. (2008) in order to better accommodate the continuum regions for the CO lines.

4 DISCUSSION

4.1 Emission lines

In order to compare the frequency of occurrence of the emission lines in our sample with what is seen in Seyfert galaxies, we show a histogram in Fig. 2 where the lines found here are compared to those of Riffel et al. (2006). What clearly emerges from this figure is that [S III], He I, and Pa β lines are less frequent in our sample (occurring in ~ 60 per cent of the sources) than in Seyferts (present in almost

all of the objects). On the other hand, we find a higher frequency of occurrence of lines of [C I] (~ 65 per cent), [P II] (~ 40 per cent), and [Fe II] (~ 65 per cent) than in Sy 1 objects, and a similar rate as in Sy 2s. The remaining emission lines occur with similar frequencies in the present sample and in Seyferts (see also Lamperti et al. 2017). Lines that are less frequent in the present sample compared to AGNs are located in regions with strong stellar features. Thus, it is possible that the absence of these features is because they are intrinsically weaker than in AGNs and/or diluted by the broad

Table 6. Absorption feature EWs (in Å).

Line	NGC 23	NGC 520	NGC 660	NGC 1055	NGC 1134	NGC 1204	NGC 1222	NGC 1266
Ca4227	0.36 ± 0.06	–	0.53 ± 0.61	–	1.14 ± 0.16	–	–	–
G4300	1.56 ± 0.19	–	5.18 ± 1.62	–	2.01 ± 0.56	–	–	–
Fe4383	1.67 ± 0.22	–	7.23 ± 0.68	–	3.84 ± 1.05	–	–	7.53 ± 2.22
Ca4455	0.49 ± 0.1	3.22 ± 0.47	2.01 ± 0.3	–	0.28 ± 0.22	–	–	–
Fe4531	2.26 ± 0.16	–	–	–	1.2 ± 0.46	–	–	–
C ₂ 4668	3.88 ± 0.2	–	–	–	4.94 ± 0.55	–	–	–
Fe5015	–	–	–	–	–	–	–	–
Mg ₁	3.84 ± 0.19	–	5.26 ± 0.3	5.2 ± 0.33	4.06 ± 0.31	4.39 ± 0.27	–	3.27 ± 0.74
Mg ₂	4.98 ± 0.13	–	6.46 ± 0.21	6.73 ± 0.2	5.36 ± 0.18	5.24 ± 0.18	–	4.14 ± 0.37
Mg _b	2.52 ± 0.15	–	2.71 ± 0.25	3.08 ± 0.26	2.9 ± 0.27	3.03 ± 0.31	0.85 ± 0.19	3.81 ± 0.5
Fe5270	1.91 ± 0.12	–	2.53 ± 0.35	1.92 ± 0.32	2.44 ± 0.2	2.09 ± 0.3	–	2.43 ± 0.45
Fe5335	1.73 ± 0.12	–	2.02 ± 0.24	1.64 ± 0.34	2.17 ± 0.2	1.48 ± 0.33	0.66 ± 0.28	2.38 ± 0.67
Fe5406	0.95 ± 0.04	–	1.0 ± 0.15	0.57 ± 0.27	1.25 ± 0.14	0.68 ± 0.3	0.09 ± 0.1	2.33 ± 0.32
Fe5709	0.64 ± 0.04	–	0.77 ± 0.1	0.72 ± 0.13	0.79 ± 0.07	0.75 ± 0.14	0.45 ± 0.04	0.74 ± 0.4
Fe5782	0.41 ± 0.04	–	1.11 ± 0.08	–	0.68 ± 0.06	0.05 ± 0.16	0.68 ± 0.18	0.98 ± 0.22
NaD	4.25 ± 0.08	1.91 ± 0.25	5.07 ± 0.19	4.02 ± 0.27	4.71 ± 0.12	3.56 ± 0.21	–	6.37 ± 0.23
TiO ₁	0.57 ± 0.09	–	–	–	–	0.51 ± 0.24	–	–
TiO ₂	3.82 ± 0.11	–	5.79 ± 0.2	7.96 ± 0.28	6.13 ± 0.2	6.07 ± 0.27	3.87 ± 0.19	8.34 ± 0.51
CaT1	4.13 ± 0.11	–	–	–	3.62 ± 0.20	1.16 ± 0.36	3.93 ± 0.13	5.74 ± 1.14
CaT2	5.48 ± 0.09	–	–	–	7.51 ± 0.17	3.11 ± 0.31	5.46 ± 0.13	6.16 ± 1.13
CaT3	3.22 ± 0.16	–	–	–	3.07 ± 0.50	–	2.97 ± 0.17	–
ZrO	16.76 ± 0.27	–	–	–	13.09 ± 1.29	15.60 ± 1.78	14.06 ± 0.56	6.70 ± 2.53
VO	0.05 ± 0.31	–	1.41 ± 0.63	–	–	–	–	–
CN11	12.32 ± 0.14	–	3.76 ± 0.28	–	11.15 ± 0.17	6.48 ± 0.31	6.37 ± 0.27	12.41 ± 0.92
NaI1.14	1.74 ± 0.08	–	2.43 ± 0.18	–	1.48 ± 0.11	1.34 ± 0.18	2.01 ± 0.06	3.46 ± 0.44
FeI1.16	0.71 ± 0.05	–	0.44 ± 0.07	–	0.21 ± 0.06	0.71 ± 0.07	0.65 ± 0.06	–
MgI1.24	0.99 ± 0.06	–	0.74 ± 0.05	–	1.68 ± 0.10	1.15 ± 0.07	–	0.57 ± 0.15
MnI1.29	0.03 ± 0.15	–	0.28 ± 0.14	–	0.06 ± 0.25	0.80 ± 0.35	0.55 ± 0.10	3.32 ± 0.14
AlI1.31	1.54 ± 0.07	–	1.93 ± 0.57	–	2.17 ± 0.10	2.16 ± 0.34	1.90 ± 0.07	3.04 ± 0.15
MgI1.48	1.80 ± 0.03	2.94 ± 0.17	1.96 ± 0.03	1.14 ± 0.25	1.67 ± 0.04	1.16 ± 0.06	1.07 ± 0.07	1.15 ± 0.11
MgI1.50	3.77 ± 0.07	3.28 ± 0.30	2.43 ± 0.10	–	4.35 ± 0.09	3.46 ± 0.08	2.44 ± 0.08	2.81 ± 0.13
CO1.5a	3.52 ± 0.09	6.51 ± 0.23	4.33 ± 0.10	5.12 ± 0.36	2.61 ± 0.23	3.18 ± 0.13	2.66 ± 0.05	5.24 ± 0.15
CO1.5b	4.26 ± 0.11	6.76 ± 0.23	4.94 ± 0.10	4.71 ± 0.19	4.44 ± 0.19	4.35 ± 0.08	2.50 ± 0.05	5.28 ± 0.07
FeI1.58	1.50 ± 0.06	3.64 ± 0.13	2.11 ± 0.06	0.45 ± 0.10	0.89 ± 0.11	1.85 ± 0.06	1.01 ± 0.04	1.66 ± 0.05
SiI1.58	3.66 ± 0.10	3.65 ± 0.24	4.03 ± 0.13	4.40 ± 0.20	3.77 ± 0.18	4.25 ± 0.11	3.00 ± 0.08	4.63 ± 0.10
CO1.5c	3.50 ± 0.06	3.39 ± 0.20	3.83 ± 0.11	3.16 ± 0.17	2.72 ± 0.10	4.07 ± 0.11	2.22 ± 0.12	4.49 ± 0.12
CO1.6a	4.97 ± 0.11	7.60 ± 0.39	6.70 ± 0.15	7.21 ± 0.44	5.43 ± 0.16	7.73 ± 0.25	4.29 ± 0.29	4.73 ± 0.30
CO1.6b	2.32 ± 0.05	3.21 ± 0.19	0.79 ± 0.07	1.11 ± 0.62	1.57 ± 0.08	1.34 ± 0.13	1.75 ± 0.07	2.92 ± 0.22
MgI1.7	1.68 ± 0.05	0.76 ± 0.21	1.37 ± 0.04	0.94 ± 0.45	0.91 ± 0.04	1.35 ± 0.08	1.16 ± 0.04	0.23 ± 0.21
NaI2.20	3.45 ± 0.08	2.51 ± 0.10	2.88 ± 0.07	4.26 ± 0.26	2.82 ± 0.08	3.24 ± 0.04	1.29 ± 0.08	3.31 ± 0.12
CaI2.26	3.07 ± 0.07	4.07 ± 0.12	2.40 ± 0.18	3.87 ± 0.39	1.78 ± 0.07	2.21 ± 0.14	2.25 ± 0.10	2.15 ± 0.08
MgI2.28	1.14 ± 0.02	1.20 ± 0.09	0.60 ± 0.04	5.57 ± 0.10	0.62 ± 0.04	0.37 ± 0.04	0.31 ± 0.06	0.03 ± 0.01
CO2.2	20.26 ± 0.56	23.16 ± 0.36	12.23 ± 0.39	23.11 ± 1.22	19.33 ± 0.41	21.80 ± 0.58	18.03 ± 0.61	24.34 ± 0.61
CO2.3a	19.07 ± 0.38	26.71 ± 0.35	12.45 ± 0.66	22.69 ± 0.80	21.93 ± 0.26	22.02 ± 0.43	18.71 ± 0.64	24.94 ± 0.40
CO2.3b	21.53 ± 0.37	27.00 ± 0.42	12.50 ± 0.78	18.28 ± 0.56	24.03 ± 0.13	22.57 ± 0.44	13.99 ± 0.85	24.52 ± 0.26

absorption features that dominate the $z + J$ band. Note though that for three objects (NGC 1055, NGC 6835, and NGC 520, see Fig. 4), our spectral range excludes the [S III], He I, and [C I] emission lines. If present in these spectra, they would show up in ~ 80 per cent of our sample.

It is worth mentioning that the kinematics of the [S III], [Fe II], and H₂ lines as well as the excitation mechanisms of the [Fe II] and H₂ lines of the galaxies of this sample were explored in Riffel et al. (2013b). However, the low-ionization forbidden lines of [C I] (i.e. λ 9850 Å) and [P II] (i.e. λ 11886 Å), also detected in our sample, were not yet analysed. Although the [P II] line is stronger compared to [Fe II] λ 12570 Å in Sy 2s (Riffel et al. 2006) than in the other types of galaxies, the detection of [P II] lines is surprising here. This is because at Solar metallicity, Phosphorus is about 1000 times less

abundant than Carbon (Ferguson et al. 1997) and 100 times less abundant than Iron (Oliva et al. 2001). Hence, if the P/C abundance is near to solar, the [P II] lines should not be present, unless other strong abundant elements are much more optically thick than they appear. A similar problem is found in some quasars for which broad absorption lines of P v $\lambda\lambda$ 1118,1128 Å are detected and extreme abundances ratios for P/C are found (Hamann 1998; Hamann et al. 2001; Borguet et al. 2012). According to Oliva et al. (2001) for a solar Fe/P ~ 100 abundance ratio, one expects that $\frac{[\text{Fe II}]}{[\text{P II}]}$ = 50, similar to what is expected for supernova remnants. The NIR [P II] emission lines may probably help to set some constraints on the abundance of Phosphorus in galaxies.

As discussed in Oliva et al. (2001) bright [Fe II] lines can only be formed in regions where hydrogen is partially ionized. Such regions

Table 7. Absorption feature EWs (in Å).

Line	UGC2982	NGC 1797	NGC 6814	NGC 6835	UGC12150	NGC 7465	NGC 7591	NGC 7678
Ca4227	–	0.91 ± 0.12	–	–	–	0.47 ± 0.1	–	–
G4300	–	1.65 ± 0.44	–	–	–	2.84 ± 0.52	–	0.78 ± 0.34
Fe4383	–	–	–	–	–	2.77 ± 0.27	–	2.24 ± 0.4
Ca4455	–	–	–	–	–	0.53 ± 0.16	–	1.11 ± 0.12
Fe4531	–	1.93 ± 0.37	–	–	–	2.67 ± 0.16	–	1.48 ± 0.32
C ₂ 4668	–	–	–	–	–	–	–	1.1 ± 0.42
Fe5015	–	–	–	–	–	–	–	–
Mg ₁	–	2.35 ± 0.21	–	–	–	–	–	3.61 ± 0.33
Mg ₂	–	3.77 ± 0.13	–	–	4.28 ± 0.26	4.07 ± 0.24	5.14 ± 0.36	4.23 ± 0.16
Mg _b	–	2.12 ± 0.24	–	–	2.04 ± 0.27	2.56 ± 0.23	3.09 ± 0.28	1.96 ± 0.23
Fe5270	–	1.32 ± 0.19	–	–	1.34 ± 0.28	1.78 ± 0.17	1.82 ± 0.29	1.31 ± 0.16
Fe5335	–	1.22 ± 0.13	–	–	1.11 ± 0.37	1.85 ± 0.15	2.32 ± 0.3	1.5 ± 0.29
Fe5406	–	0.87 ± 0.11	–	–	0.44 ± 0.2	0.78 ± 0.15	1.31 ± 0.21	1.04 ± 0.12
Fe5709	–	0.35 ± 0.06	–	–	0.64 ± 0.1	0.7 ± 0.06	1.14 ± 0.17	0.78 ± 0.11
Fe5782	–	0.31 ± 0.06	–	–	–	0.57 ± 0.03	0.61 ± 0.14	0.86 ± 0.09
NaD	4.78 ± 0.37	6.27 ± 0.19	–	–	7.47 ± 0.52	1.67 ± 0.27	3.86 ± 0.19	4.17 ± 0.25
TiO ₁	–	–	–	–	–	1.4 ± 0.16	–	–
TiO ₂	–	2.08 ± 0.23	–	–	4.88 ± 0.52	4.63 ± 0.15	3.4 ± 0.25	4.6 ± 0.21
CaT1	–	1.13 ± 0.39	–	–	2.22 ± 0.42	5.17 ± 0.17	0.80 ± 0.33	2.73 ± 0.26
CaT2	–	3.16 ± 0.34	0.36 ± 0.19	–	1.55 ± 0.43	6.28 ± 0.14	5.37 ± 0.26	4.29 ± 0.24
CaT3	–	–	3.35 ± 0.06	–	–	5.93 ± 0.33	3.73 ± 0.39	5.90 ± 0.26
ZrO	–	15.11 ± 2.04	1.20 ± 1.74	–	12.38 ± 0.98	9.16 ± 0.75	14.76 ± 1.61	6.18 ± 1.10
VO	7.10 ± 1.35	–	3.89 ± 0.43	–	1.13 ± 0.43	–	–	–
CN11	20.92 ± 0.74	6.49 ± 0.33	–	–	7.95 ± 0.42	6.91 ± 0.37	11.93 ± 0.34	5.08 ± 0.72
NaI1.14	–	1.38 ± 0.19	3.99 ± 0.13	7.92 ± 0.83	1.75 ± 0.15	1.66 ± 0.18	1.17 ± 0.22	0.78 ± 0.11
FeI1.16	0.17 ± 0.20	0.70 ± 0.07	0.53 ± 0.06	2.78 ± 0.11	0.68 ± 0.08	0.76 ± 0.06	1.25 ± 0.06	–
MgI1.24	1.40 ± 0.06	1.16 ± 0.07	0.76 ± 0.05	1.49 ± 0.06	0.71 ± 0.15	0.63 ± 0.04	0.67 ± 0.02	0.41 ± 0.06
MnI1.29	3.11 ± 0.62	0.77 ± 0.33	10.00 ± 0.43	1.53 ± 0.11	1.74 ± 0.14	1.12 ± 0.10	–	2.18 ± 0.20
AlI1.31	0.46 ± 0.26	2.15 ± 0.35	1.33 ± 0.11	–	3.16 ± 0.34	2.29 ± 0.15	2.89 ± 0.16	2.84 ± 0.17
MgI1.48	0.57 ± 0.10	1.16 ± 0.07	0.94 ± 0.03	1.83 ± 0.14	0.80 ± 0.10	1.83 ± 0.09	1.38 ± 0.05	1.77 ± 0.08
MgI1.50	2.41 ± 0.10	3.46 ± 0.08	2.07 ± 0.07	1.82 ± 0.25	2.88 ± 0.18	3.12 ± 0.17	3.11 ± 0.14	3.53 ± 0.14
CO1.5a	2.83 ± 0.05	3.21 ± 0.10	2.53 ± 0.07	3.06 ± 0.07	4.03 ± 0.11	3.89 ± 0.07	4.39 ± 0.13	2.98 ± 0.09
CO1.5b	3.46 ± 0.04	4.34 ± 0.07	3.10 ± 0.05	4.63 ± 0.19	5.34 ± 0.13	3.48 ± 0.09	4.55 ± 0.10	3.52 ± 0.06
FeI1.58	0.73 ± 0.03	1.85 ± 0.05	0.77 ± 0.03	2.46 ± 0.11	1.80 ± 0.09	1.35 ± 0.06	1.81 ± 0.07	1.18 ± 0.05
SiI1.58	2.81 ± 0.07	4.25 ± 0.12	2.57 ± 0.07	4.45 ± 0.19	4.58 ± 0.17	3.43 ± 0.11	3.71 ± 0.15	2.01 ± 0.14
CO1.5c	2.99 ± 0.07	4.09 ± 0.10	2.51 ± 0.06	3.46 ± 0.18	3.39 ± 0.13	2.93 ± 0.13	4.03 ± 0.19	2.70 ± 0.16
CO1.6a	6.02 ± 0.19	7.73 ± 0.27	4.26 ± 0.20	9.42 ± 0.45	7.24 ± 0.18	6.17 ± 0.20	7.73 ± 0.26	6.50 ± 0.28
CO1.6b	2.64 ± 0.13	1.36 ± 0.12	0.92 ± 0.05	2.07 ± 0.28	–	1.13 ± 0.09	1.66 ± 0.10	–
MgI1.7	0.85 ± 0.11	1.35 ± 0.09	1.11 ± 0.03	2.21 ± 0.29	1.34 ± 0.14	1.82 ± 0.05	1.76 ± 0.07	1.73 ± 0.04
NaI2.20	4.15 ± 0.15	3.24 ± 0.05	1.54 ± 0.03	3.41 ± 0.04	4.10 ± 0.07	2.70 ± 0.04	3.63 ± 0.08	2.88 ± 0.07
CaI2.26	6.74 ± 0.13	2.21 ± 0.16	1.04 ± 0.04	2.43 ± 0.04	4.37 ± 0.25	1.87 ± 0.09	4.35 ± 0.11	2.49 ± 0.13
MgI2.28	0.71 ± 0.18	0.36 ± 0.04	0.05 ± 0.04	1.05 ± 0.04	–	0.33 ± 0.05	1.58 ± 0.05	0.86 ± 0.06
CO2.2	17.96 ± 0.81	21.54 ± 0.56	6.24 ± 0.12	22.26 ± 0.54	22.08 ± 1.02	16.14 ± 0.67	23.89 ± 0.47	17.53 ± 0.83
CO2.3a	22.66 ± 1.19	22.13 ± 0.39	2.96 ± 0.16	23.54 ± 0.41	22.84 ± 0.95	14.90 ± 0.82	26.34 ± 0.40	24.72 ± 0.77
CO2.3b	27.53 ± 1.39	22.58 ± 0.44	4.36 ± 0.20	24.65 ± 0.41	20.18 ± 1.07	14.97 ± 1.47	27.79 ± 0.50	20.27 ± 0.89

of hot, partially ionized gas can only be produced in an efficient way by shocks and/or photoionization by soft X-rays. According to these authors, [Fe II]/[P II] can be used to distinguish between shocks (ratio $\gtrsim 20$) and photoionization (ratio $\lesssim 2$). In order to test this hypothesis, we plotted in Fig. 6 [Fe II]/[P II] \times [C I]/[P II] for our sample as well as the Seyfert galaxies of Riffel et al. (2006). As can be seen in this figure, there is a good correlation and no clear separation between the SFGs and the Seyferts, suggesting that the dominant excitation mechanism is the same for the three ions. Furthermore, due to the low values derived for the [Fe II]/[P II] ratio, that excitation mechanism might be expected to be photoionization based on the arguments of Oliva et al. (2001). To test this, we have

computed photoionization models using CLOUDY/C17.01⁴ (Ferland et al. 2017) updated with the next release of collisional strengths for [P II] (taken from Tayal 2004) as well as with new transition probabilities⁵ (private communication), however these models are not able to reproduce the observed line ratios, underestimating both (the models values for both ratios are nearly zero). This may be due to the fact that these lines are not in fact excited by photoionization, but mostly driven by shocks.

⁴Available at: <https://www.nublado.org>.

⁵They are a combination of data taken from the MCHF/MCDHF data base at <http://nlte.nist.gov/MCHF/> and data from the NIST Atomic Spectra Database at <https://www.nist.gov/pml/atomic-spectra-database>.

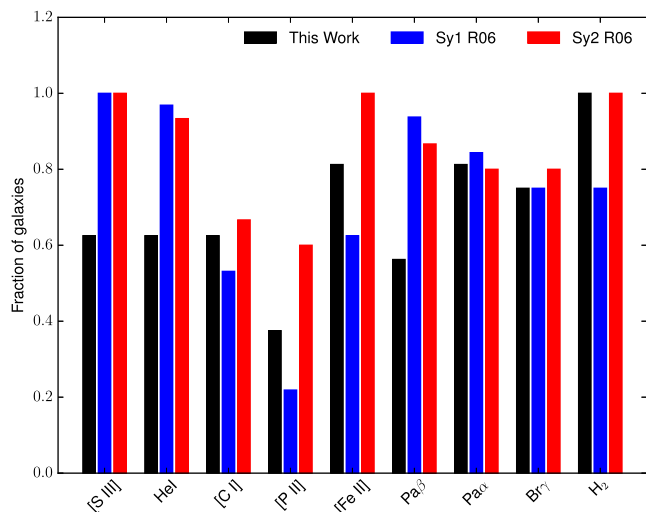


Figure 2. Histogram showing statistics of the most common NIR emission lines.

4.2 Absorption features

It is crucial to be able to derive ages and chemical composition in order to understand the dominant underlying unresolved stellar content of galaxies (Röck et al. 2017). So far, the NIR is lacking a clear procedure based on absorption-line strengths. The obvious choice to do this kind of study is using stellar clusters as probes, instead of the use of more complex star-forming objects. However, while observations of the integrated spectra of stellar clusters in the optical region have been available for almost 30 yr (e.g. Bica 1988), in the NIR such observations are very difficult since the light emitted by the stars of the clusters in the NIR bands is dominated by a few very bright stellar phases making it difficult to get reliable integrated spectra of such objects in the NIR (e.g. Lyubenova et al. 2010; Riffel et al. 2011c).

In order to have a more homogeneous data set, in addition to the data set we present here representing complex SFHs of SFGs (Section 2), we collected spectra of nearby ETGs (which tend to have less complex SFHs than our sample) observed similarly as those in this work. Our final data set representing the older stellar population is composed of 12 ETGs selected in order to span a wide range of ages (1–15 Gyr) at approximately solar metallicity and observed by Baldwin et al. (2017) using Gemini/GNIRS in the cross-dispersed mode ($\sim 0.8\text{--}2.5\ \mu\text{m}$; $R \sim 1700$; $\sigma \sim 75\ \text{km s}^{-1}$) plus six ETGs selected from the Calar Alto Legacy Integral Field Area Survey (CALIFA Sánchez et al. 2016) and observed by Dahmer-Hahn et al. (2018) using the TripleSpec spectrograph attached to the Astrophysical Research Consortium (ARC) 3.5-m telescope ($\sim 0.95\text{--}2.45\ \mu\text{m}$; $R \sim 2000$; $\sigma \sim 64\ \text{km s}^{-1}$). In addition to these NIR spectra, we also collected, when available, the optical spectra of the sources. In the case of Baldwin et al. (2017) galaxies, the optical spectra were taken from the Sloan Digital Sky Survey (Ahn et al. 2014), while for the sample of Dahmer-Hahn et al. (2018) we took the data from the CALIFA Sánchez et al. (2016). The optical and NIR indices were measured by us using the definitions of Table 5 and are listed as online material in Tables B1, B2, and B3.

4.2.1 Previous NIR index–index correlations

Due to the lack of adequate data sets to test predictions of NIR data, compared to the optical (see Thomas, Maraston & Bender 2003, for example), there are only a few studies trying to understand the behaviour of NIR \times NIR indices. For instance, Mármol-Queraltó et al. (2009) studied a sample of ETGs and found a strong correlation between C_{24668} and $NaI_{2.20}$ indices. In Fig. 7a we show the Mármol-Queraltó et al. (2009) measurements (open diamonds) and the literature compilation presented by Röck et al. (plus symbols, 2017) together with our data (squares). Even though we only measured both indices for four sources, this correlation seems to still hold for SFGs, which populate the lower left end of the correlation (Fig. 7a).

Using a similar approach, Cesetti et al. (2009) reported a trend of correlation of the optical Mg_2 band with NIR indexes, such as $NaI_{2.20}$, $CaI_{2.26}$, and $CO_{2.2}$ for ETGs. In Figs 7(b)–(d) we plotted our sample (filled squares), together with those of Cesetti et al. (2009, open diamonds) and Kotilainen et al. (2012, open triangles) for early-type sources. Additionally we also added the inactive spirals (octagons, LTG-K12) of Kotilainen et al. (2012). From Fig. 7d we have excluded the two Seyfert galaxies (NGC 660 and NGC 6814) since the CO band can be very diluted in these kind of sources (Riffel et al. 2009; Burtscher et al. 2015).

From Fig. 7 it is clear that the trend seems to hold for $NaI_{2.20} \times Mg_2$, while for $CaI_{2.26} \times Mg_2$ there is no clear correlation, and in the case of $CO_{2.2} \times Mg_2$ instead of a positive correlation there seems to be an inverse correlation. Additionally there seems to be a segregation between early- and late-type galaxies in this plot (panel d). This indicates that CO is enhanced in younger stellar populations, in agreement with the predictions of the Maraston (2005) models as shown in Riffel et al. (2007).

To help in the interpretation of these results, on these index–index diagrams we have overplotted the new optical-to-NIR IRTF-based stellar population synthesis models of the E-MILES team (Vazdekis et al. 2012, 2016; Röck et al. 2016). The models employed are those computed using the PADOVA isochrones (Girardi et al. 2000), with ages in the range $0.3\ \text{Gyr} < t < 15.0\ \text{Gyr}$ and metallicities within $[Fe/H] = -0.40$, $[Fe/H] = 0.00$, and $[Fe/H] = 0.22$ with two different spectral resolutions ($\sigma = 60\ \text{km s}^{-1}$ and $\sigma = 228\ \text{km s}^{-1}$, the shaded area represents the differences caused by σ). We also plotted TP-AGB heavy (see Zibetti et al. 2013, for a comparison between TP-AGB heavy and light models), Pickles-based models of Maraston & Strömbäck (2011, M11 hereafter), which do have the same prescription than Maraston (2005) models but with a higher spectral resolution ($R = 500$) than the 2005 models, therefore making them more suitable for our comparisons. However, it is important to have in mind that M11 models do have a poorer spectral resolution than our data, the effects on the indices strengths by degrading the resolution to M11 models is within the uncertainties of our measurements. These models are shown as open brown stars and are only available for solar metallicity. What emerges from this exercise is that the models in general are not able to predict the NIR indices and that there is a segregation between early- (open diamonds and plus markers) and late-type (filled squares and octagons) galaxies in these diagrams. The upper panels show significantly larger $NaI_{2.20}$ index values than predicted by the models with standard initial mass function (IMF). Both the optical Mg - and C -dominated indices are stronger than the models for the most massive galaxies (i.e. the ones with the largest index values). In the case of the $NaI_{2.20}$ index, Röck et al. (2017) concluded that for early-type sources the large values

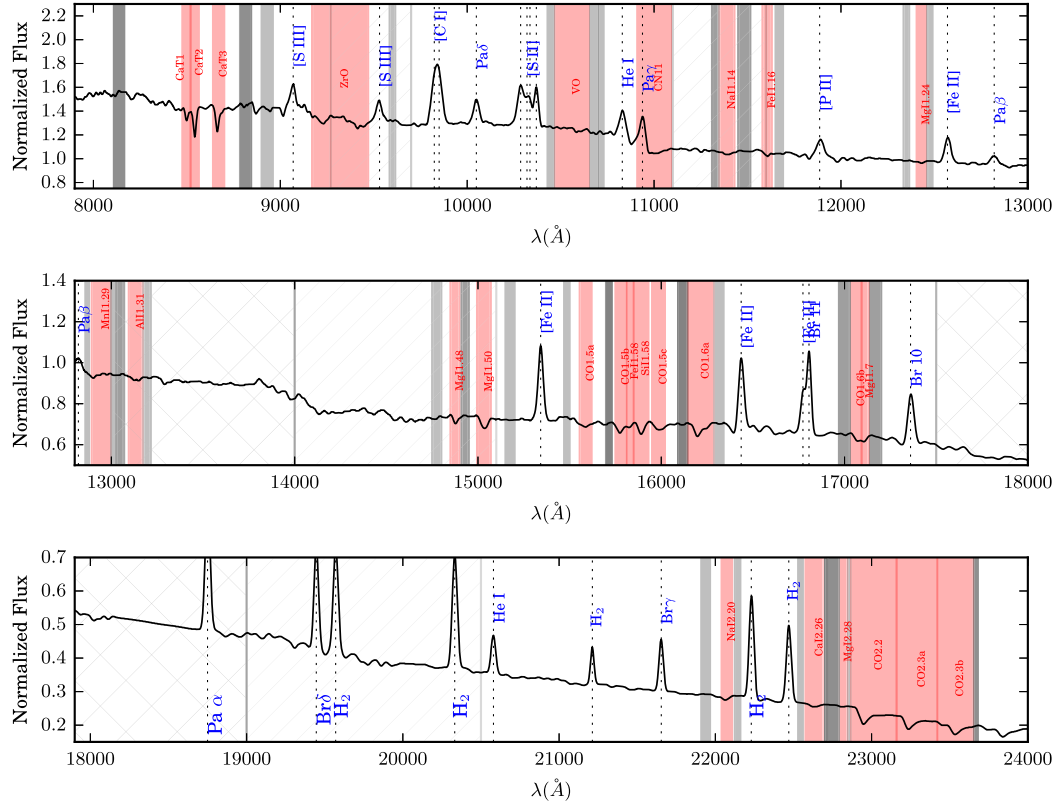


Figure 3. Simulated spectrum showing the NIR indices definitions. The blue and red continuum band passes are in grey and line limits in red. Regions of strong (transmission <20 per cent) telluric absorption are shaded with an ‘X’ pattern, while regions of moderate (transmission <80 per cent) telluric absorption are shaded with a line pattern. Emission lines and absorption features are labelled. See the text for details.

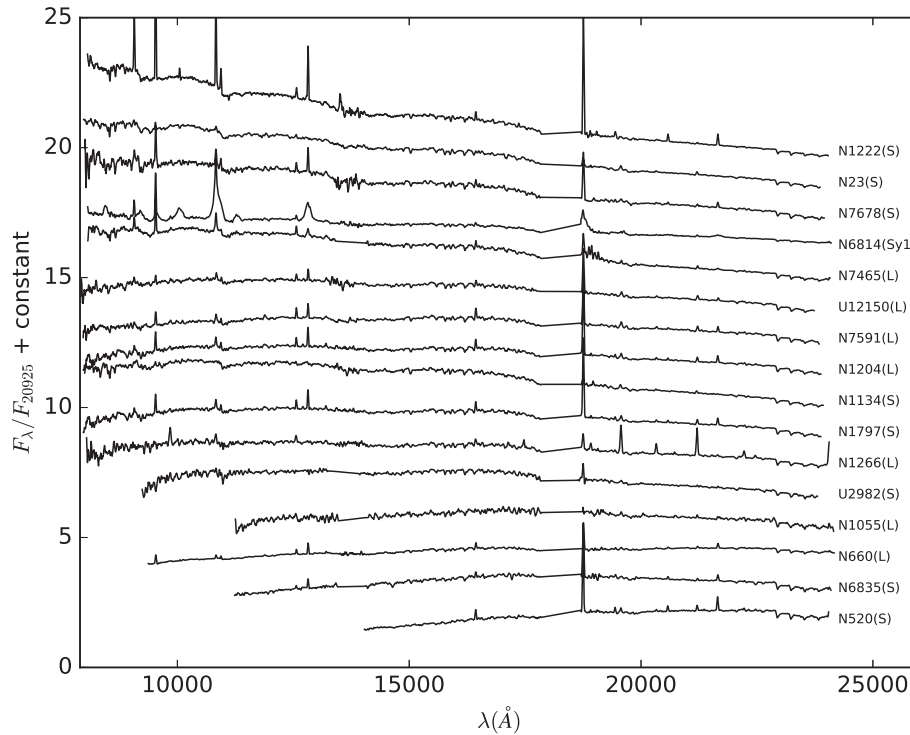


Figure 4. Near-infrared normalized spectra ordered according to their shapes from steeper (top) to flatter (bottom). The data were normalized at 20 925 Å. Activity types are listed (S = SFG and L = LINER).

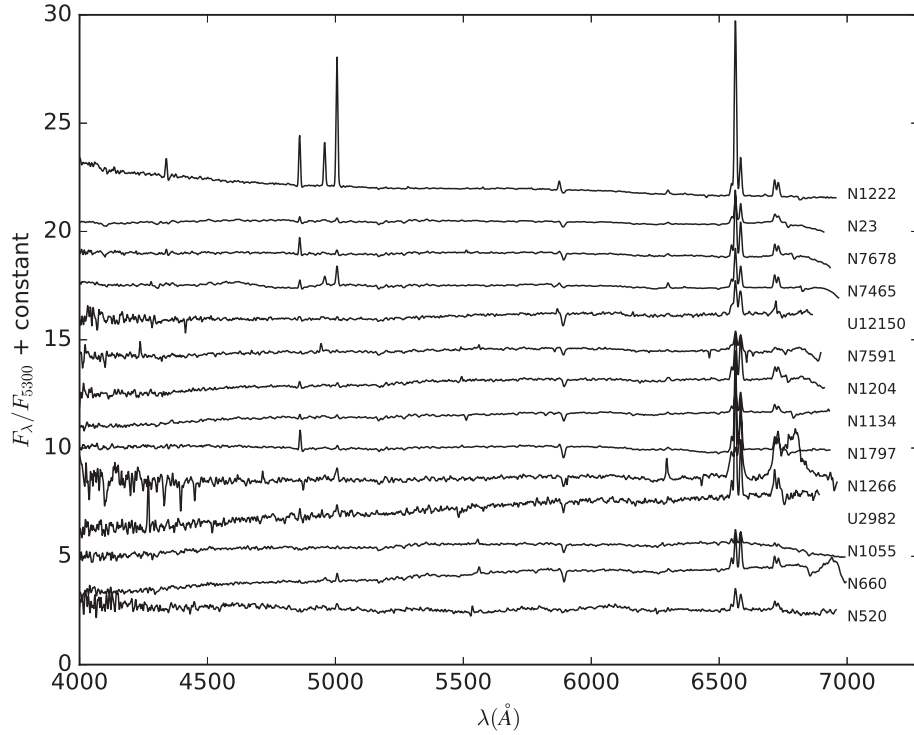


Figure 5. Same order as Fig. 4, but for the optical spectral range. The data were normalized at 5300 Å.

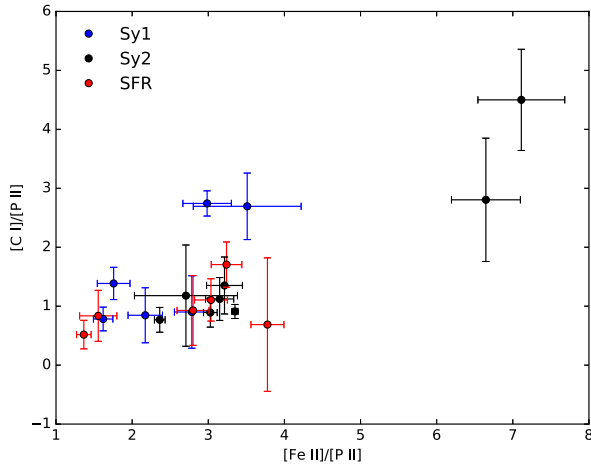


Figure 6. The correlation between the emission-line ratios of [C I] $\lambda 9850$ Å and [Fe II] $\lambda 12570$ Å relative to [P II] $\lambda 11886$ Å.

obtained for this index are due to a combination of a bottom-heavy IMF and the [Na/Fe] abundances. On the other hand, Alton et al. (2018) found that their sample of massive ETGs is consistent with having a Milky Way-like IMF, or at most a modestly bottom-heavy IMF, and suggested that their extreme abundance values for Na, in the cores of massive ETGs, may be explained by the metallicity-dependent nucleosynthetic yield of Na.

The lower panels of Fig. 7 show that the ETGs are in better agreement with the predicted values. However, about half of our SFGs sample show stronger CaI2.26 and CO2.2 values than predicted by the models. From these plots, we can also infer that the TP-AGB phase does not change substantially the CO index, once the solar metallicity M11 models are in agreement with the E-MILES

ones for the younger ages ($t \lesssim 1$ Gyr), with a large discrepancy for the older ages. Besides age, metallicity appears as an additional discriminator for the measured strengths of CO bands, with low metallicity ($[\text{Fe}/\text{H}] = -0.40$) and intermediate ages (~ 350 Myr) showing the largest values for the CO2.2 index. This is in agreement with the previous findings of Kotilainen et al. (2012), who found that the evolved red stars completely dominate the NIR spectra, and that in this age range, the hot, young stars contribution to the EWs is virtually non-existent. So far, to fully access these younger stellar content of the galaxies it is necessary to fit the full spectrum, taking the continuum into account (see Baldwin et al. 2017; Dahmer-Hahn et al. 2018, for example). However, this is beyond the scope of this paper and will be the subject of a future investigation (Riffel et al., in preparation). On the other hand, the lower values of the CO index presented by the ETGs are also not explained by the models, with M11 models underestimating and E-MILES models overestimating the main locus occupied by these sources.

4.2.2 New index–index correlations

Because we measured a large set of lines for our sample, we have tried to find new correlations among the different absorption features by plotting all the EWs listed in Tables 6 and 7, as well as literature data (Tables B1 to B3) against each other. From these, we removed the correlations already discussed above (Fig. 7) as well as the optical \times optical indices correlations since these are well studied.⁶ Since the CaT lines are correlated (e.g. Cenarro et al. 2001), we only used CaT2 in our search for correlations. The final set of optical

⁶The NaI2.20 and CO2.2 are well studied, however, we decided to keep them here for diagrams distinct from those presented in Fig. 7 because correlations with other lines may help to shed some light in the understanding of the mechanisms driving these lines.

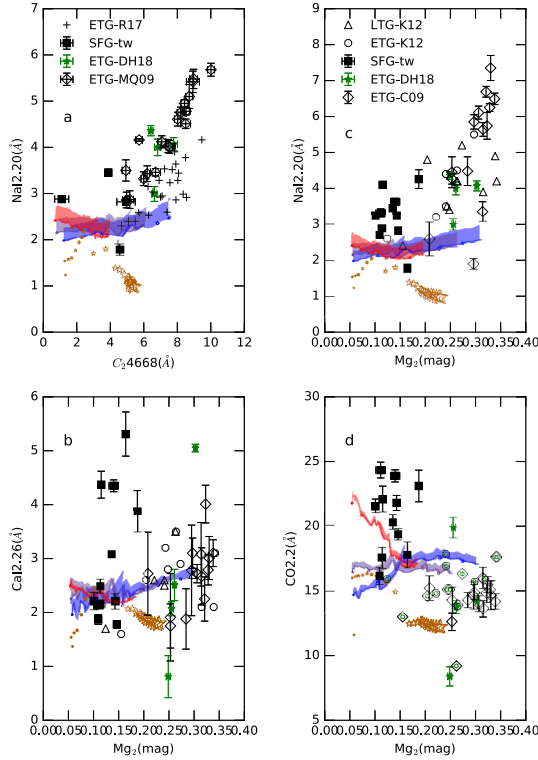


Figure 7. Index–index diagrams. The filled boxes are from this work. The plus markers indicate early-type objects indices presented in Röck et al. (2017, panel a, R17). The open diamonds are indices measured in ETGs taken from Mármol-Queraltó et al. (panel a, ETG-MQ09 2009) and Cesetti et al. (panels b, c, and d, ETG-C09 2009). The triangles and octagons represent, respectively, the late and ETGs studied by Kotilainen et al. (2012, LTG-K12 and ETG-K12). The filled green stars represent our new measurements for the ETGs of Dahmer-Hahn et al. (2018, ETG-DH18) in all panels. Note that the literature data may have different definitions among themselves and with the measurements we present here. The open brown stars represent Maraston & Strömbäck (2011) solar metallicity, Pickles-based models, with the size of the points scaling with ages (smallest points for 300 Myr and largest for 15 Gyr). The shaded areas represent IRTF-based EMILES models (Röck 2015; Röck et al. 2016; Vazdekis et al. 2016) with red, grey, and blue indicating $[\text{Fe}/\text{H}] = -0.40$, $[\text{Fe}/\text{H}] = 0.00$, and $[\text{Fe}/\text{H}] = 0.22$, respectively. The shaded area represents models with a spectral resolution of $\sigma = 60 \text{ km s}^{-1}$ (the lowest available) to $\sigma = 228 \text{ km s}^{-1}$. The age range used is between 0.3 and 15.0 Gyr, with arrows, triangles, diamonds, and pentagons representing 0.3, 1, 5, and 10 Gyr, respectively. The E-MILES models with ages smaller than 1 Gyr should be taken with caution. For more details see the text.

versus NIR and NIR versus NIR indices correlations are shown in Figs 8 and 9, together with a linear regression using the orthogonal distance regression (ODR) method that takes errors both in the x and y variables into account (Boggs & Rogers 1990). We note that when it was not possible to measure one of the indices used in the correlations, we have removed the galaxy from the plots and regression. In addition, we only considered the cases where both indices were measured at least for six sources. To help understand these plots we have overplotted the same model set as discussed above.

What emerges from Fig. 8 is that both model sets are able to predict well all the measured values for the optical indices. In the NIR, however, the models fail in their predictions, except for CO2.2 and ZrO, with E-MILES making better predictions of strengths

than M11, especially in the case of atomic absorption features. In addition, there is a clear separation of the ETGs and SFGs on the $\text{G4300} \times \text{MgI1.7}$, $\text{G4300} \times \text{NaI2.20}$, $\text{Fe4531} \times \text{MgI1.7}$, and $\text{Mg}_1 \times \text{NaI2.20}$ diagrams with ETGs in general showing higher values for both optical and NIR indices. A less evident separation of ETGs and SFGs is observed on the $\text{G4300} \times \text{CO2.2}$ and $\text{Mg}_b \times \text{NaI2.20}$ diagrams, while no separation is observed for the $\text{Fe5782} \times \text{ZrO}$ and $\text{TiO}_1 \times \text{CO2.2}$ diagrams.

The optical indices (G4300 , Fe4531 , and Mg_1) are not very sensitive to the α/Fe ratio while G4300 is mainly sensitive to the C and O abundances (Thomas et al. 2003). This may indicate that the MgI1.7 and NaI2.20 indices are also sensitive to C and/or O abundances. This is also in agreement with the findings of Röck et al. (2017) who suggested that $[\text{C}/\text{Fe}]$ enhancement might contribute to the values observed for NaI2.20 in ETGs. However, the good correlation of NaI with Mg_b may also indicate that this index is α/Fe dependent, since Mg_b is sensitive to changes in the α/Fe ratio (Thomas et al. 2003). The CO2.2 index values are well described by the model predictions for both SFGs and ETGs, with an age-metallicity dependence for the SFGs and no evidence of strong changes on their strengths caused by the amount of TP-AGB stars (see above). This is additionally supported by the $\text{CO2.2} \times \text{TiO}_1$ diagram, where M11 models, independent of age, do populate the locus filled by the ETGs, while E-MILES models do not reproduce the larger TiO and smallest CO strengths. The CO and TiO_1 correlation is not unexpected since these absorptions depend on O being available. The models do show that ZrO is more metallicity dependent while TiO_1 seems to be age dependent. In addition, some ETG show TiO_1 values larger than the models (specially E-MILES models), which can be interpreted as an IMF effect (see La Barbera et al. 2013). In the case of the Mg-dominated indices (in the NIR and optical) the large values for these indices can be associated with the most massive ETGs, and can be explained by an $[\text{Mg}/\text{Fe}]$ enhancement (e.g. Worthey, Faber & Gonzalez 1992; Martín-Navarro et al. 2018).

The correlations found from this exercise for the NIR indices are shown in Fig. 9. One particularly relevant correlation is $\text{CO1.6b} \times \text{CN11}$, as the CN11 index is believed to be heavily dominated by the AGB evolutionary phase and particularly by C stars (Maraston 2005). Almost 50 per cent of our SFG do show $\text{CN11} \gtrsim 10 \text{ Å}$, with a mean value ~ 20 per cent larger than in ETG (see Fig. 13) and are consistent with the intermediate-age (0.3–2 Gyr) models. M11 models do cover better the space of values of the measurements, but all the older ages M11 models ($t \gtrsim 3 \text{ Gyr}$) do predict more or less constant values for CN11 (the same happens for CO1.6b). The ETGs are more or less matched by SSP models with old ages and no indication of an intermediate-age population is required to explain the absorption features of these sources, once, their strengths in some cases are smaller than those of the older E-MILES SSPs. The CO2.2 and CO2.3a,b (also CO1.5a and CO1.5b) indices are to some extent described by the models, with larger values predicted for intermediate-age SSPs. The remaining strengths are not predicted by the models and no clear separation is found for SFGs and ETGs.

With the aim of understanding the behaviour of the NIR indices, we plotted them against the $[\text{Mg}/\text{Fe}]$ index of Thomas et al. (2003) defined as:

$$[\text{Mg}/\text{Fe}]' \equiv \sqrt{\text{Mg}b(0.72 \times \text{Fe5270} + 028 \times \text{Fe5335})} \quad (1)$$

which, for this sample with a small range in metallicity, is basically an age-indicator and is completely independent of the α/Fe ratio. Assuming that the ETGs used here are objects with relatively normal old stellar populations, which is a valid assumption since their full

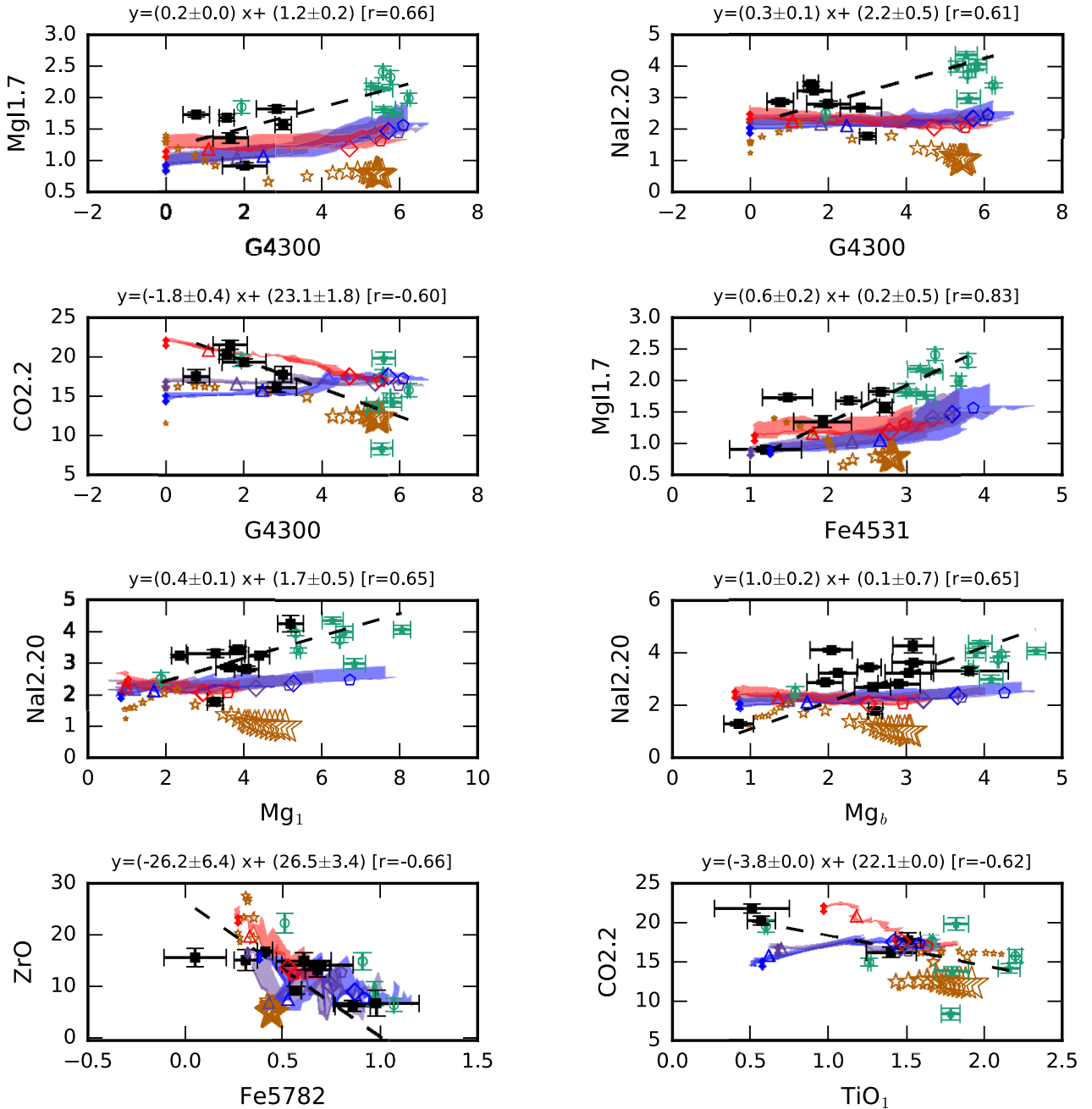
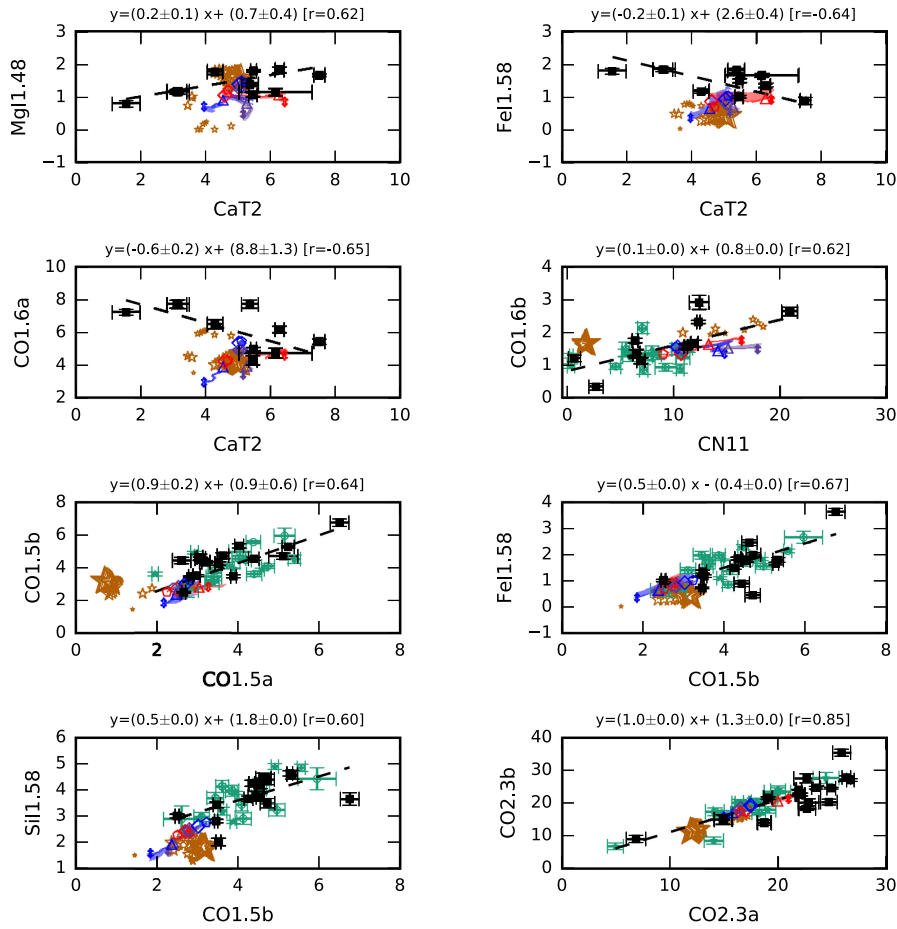
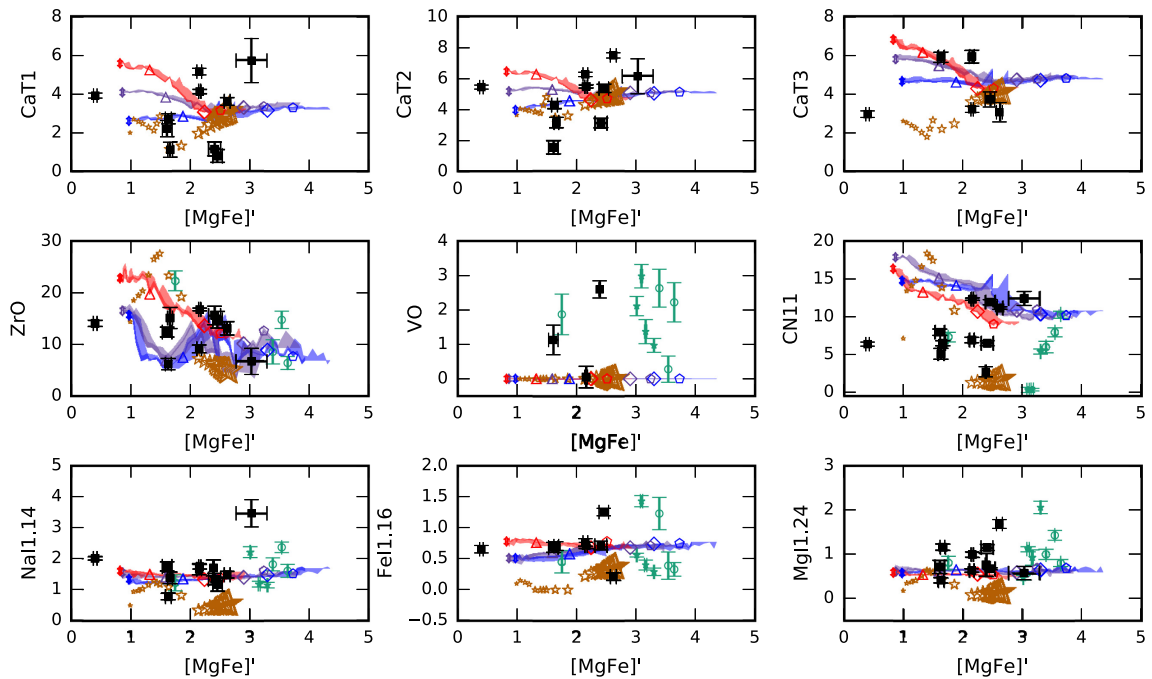


Figure 8. Index–index correlations. The black squares are the data points of this work. The green diamonds are from Baldwin et al. (2017) and filled green stars are from Dahmer-Hahn et al. (2018). The open brown stars represent Maraston & Strömbäck (2011) solar metallicity, Pickles-based models, with the size of the points scaling with ages (smallest points for 300 Myr and largest for 15 Gyr). The shaded areas represent IRTF-based EMILES models (Röck 2015; Röck et al. 2016; Vazdekis et al. 2016) with red, grey, and blue representing $[\text{Fe}/\text{H}] = -0.40$, $[\text{Fe}/\text{H}] = 0.00$, and $[\text{Fe}/\text{H}] = 0.22$, respectively. The shaded area represents models with a spectral resolution of $\sigma = 60 \text{ km s}^{-1}$ (the lowest available) to $\sigma = 228 \text{ km s}^{-1}$. The age range used is between 0.3 and 15.0 Gyr, with arrows, triangles, diamonds, and pentagons representing 0.3, 1, 5, and 10 Gyr, respectively. The models with ages smaller than 1 Gyr should be taken with caution. For more details see the text.

spectra can be well fitted with SSP models (see Baldwin et al. 2017; Dahmer-Hahn et al. 2018, for details). This can also be seen in Figs 10 to 12, where the ETGs do in general show less scatter in the $[\text{MgFe}]'$ index than the SFGs. This indicates a more complex SFH for the latter, most likely with a strong contribution from intermediate (~ 1 Gyr) stellar populations. In order to test the effect of a more complex SFH on the NIR strengths, we show in Fig. 13 histograms comparing the strength distributions between

SFG and ETG. Except for a few indices (ZrO, MgI1.48, MgI1.50, CO1.5a, FeI1.58, CO1.5c, MgI1.7, NaI2.20), the mean value for SFG is larger than that for ETG. This more complex SFH can also explain why the CN and CO bands are in general stronger for the SFGs than the ETGs. These bands are enhanced by the short-lived younger red giant branch (RGB) and TP-AGB stars (Maraston 2005; Riffel et al. 2007, 2015). According to Maraston (1998), these stars can be responsible for up to 70 per cent of the

Figure 9. Same as Fig. 8 but for NIR \times NIR indices.Figure 10. Comparison of NIR indices with $[MgFe]'$. The models are the same as Fig. 8.

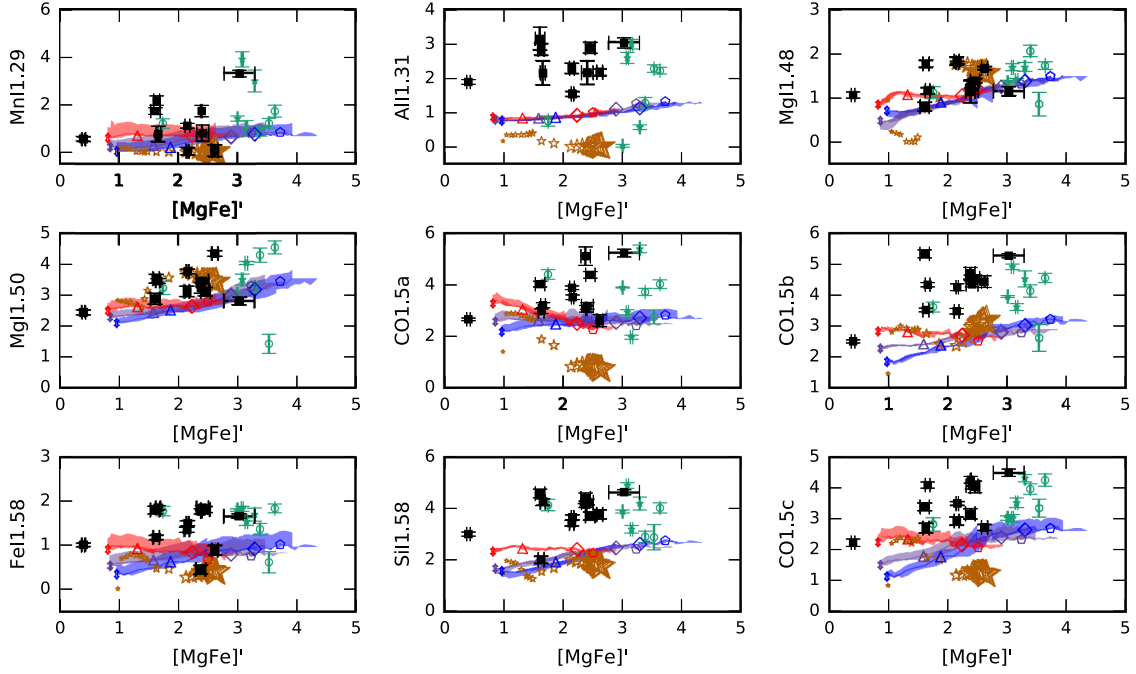


Figure 11. Comparison of NIR indices with $[MgFe]'$. The models are the same as Fig. 8.

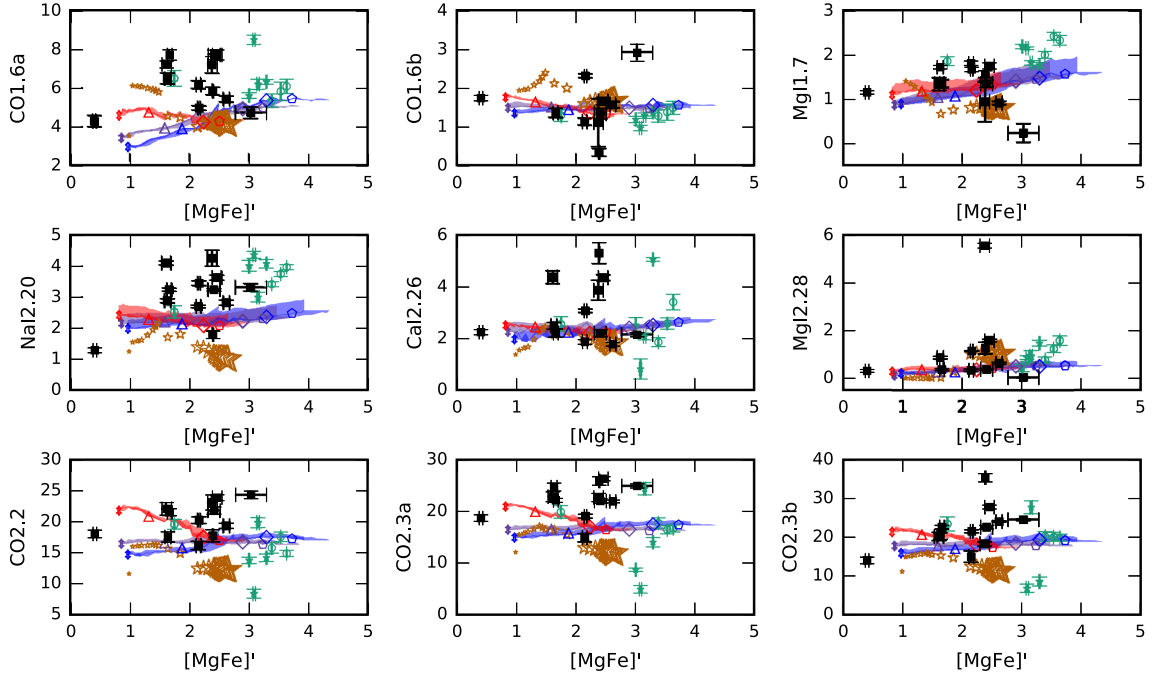


Figure 12. Comparison of NIR indices with $[MgFe]'$. The models are the same as Fig. 8.

total flux in the NIR. However, for the case of the NaI2.20 index, Röck et al. (2017) constructed models using enhanced contribution from AGB stars and found that these stars have only a very limited effect on the model predictions and do not improve significantly the fit of the model NaI2.20 indices. They also show that small fractions (3 per cent) do have a similar impact on NaI2.20 than those with larger amounts of these stars. This result is consistent

with our findings that NaI2.20 index has a mean value ~ 20 per cent larger in ETG than in SFG.

In general, the NIR line strengths are not well reproduced by any set of models, suggesting that the SFH of the galaxies cannot be recovered when only using NIR indices. Our results are in agreement with the finding of Baldwin et al. (2017) who have studied the SFH of a sample of ETG by fitting different SSP models and found

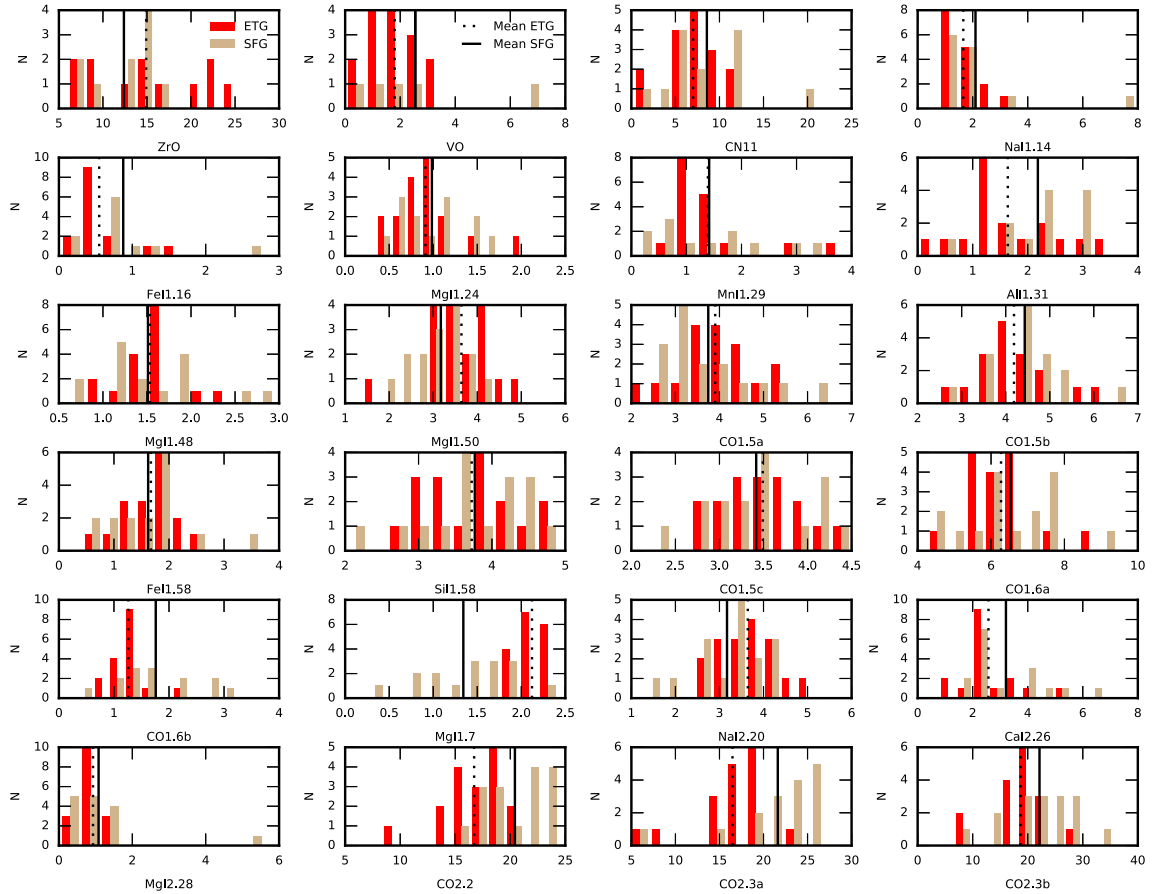


Figure 13. Comparison of NIR indices strengths between SFG and ETG.

that the SFH vary dramatically among the different EPS models when fitting NIR data, with higher spectral resolution models producing more consistent results. They also found variations in ages in the NIR tend to be small, and largely encoded in the shape of the continuum. This was also noticed in Riffel et al. (2015) who suggested that TP-AGB stars contribute noticeably to a mean stacked NIR spectrum made up with mostly late-type galaxies hosting a low-luminosity AGN, from the Palomar survey (Mason et al. 2015). This result was obtained by fitting a mix of individual IRTF stars to the mean galaxy spectrum. Nevertheless, in this same work we have shown that other evolved stars (red giants, C-R, and E-AGB stars) can reproduce most of the absorption features detected, without having to resort to stars in the TP-AGB phase.

5 FINAL REMARKS

We analysed long-slit spectra spanning optical to NIR wavelengths of 16 infrared-luminous star-forming galaxies with the aim of offering the community a set of emission and absorption feature measurements that can be used to test the predictions of the forthcoming generations of stellar population models. The optical and NIR spectra were obtained at WIRO and at SpeX/IRTF, respectively. In addition to these, we collected literature spectra of ETGs and performed the EW measurements using a new homogeneous set of continuum and band pass definitions. The main findings can be summarized as follows:

(i) All our sources display H_2 emission, characteristic of the star-forming nature of our sample. In the optical they clearly display H I emission lines. However, NGC 1055 and NGC 1134 show an NIR spectrum free of H I emission lines. We interpret this latter result as the result of the low sensitivity of the NIR detector in this wavelength interval, thus the expected $Br\gamma$ fluxes are below the detection limit.

(ii) The continua are dominated by stellar absorption features. The most common features are due to Ca I, Ca II, Fe I, Na I, Mg I, plus prominent absorption bands of: TiO, VO, ZrO, and CO. In most cases (70 per cent) the stellar continua also show evidence of dust extinction.

(iii) We present new definitions of continuum and line band passes for the NIR absorption lines. These definitions were made taking into account the position of the most common emission lines detected in this wavelength range.

(iv) We report EW measurements for 45 indices, including both optical and NIR features. We also present measurements for most of these indices in spectra of ETGs taken from literature. To the best of our knowledge, they represent the most complete set of EW measurements reported in the literature to date, and can be used to test the predictions of stellar population models from the optical to the NIR.

(v) We looked for correlations among the different absorption features, presenting as the most robust ones those with a Pearson correlation coefficient $r > 0.6$. In addition to the already known correlations in the optical region, we propose here correlations between optical and NIR indices, as well as correlations be-

tween different NIR indices, and compare them with model predictions.

(vi) While for the optical absorption features the new generation of models, with scaled-solar abundance ratios and standard IMF, share the same locus as the observed data points, they fail to predict the strengths of most of the NIR indices for the SFGs, while in the case of the early-type sources they roughly reproduce the observations. This may indicate more complex SFHs for the SFGs, which we interpreted as a strong contribution from the younger stellar populations, thus explaining the fact that the CN and CO bands are in general larger for the SFGs than the ETGs. These bands are enhanced in stars in the TP-AGB phase, however, they seems to have a limited impact on the indices of ETGs.

ACKNOWLEDGEMENTS

We are grateful to the referee for insight that has improved the quality of this paper. RR and RAR thank CNPq, CAPES, and FAPERGS for financial support for this project and to Luis Colina for helpful discussions on this project. The authors are also grateful to Richard McDermid and Christina Baldwin for kindly offering information on the ETGs used in this work, as well as, to Jari Kotilainen for sharing information on his sample of objects. We also thank Peter van Hoof for providing the new collisional strengths for [P II] lines, which will be part of the new CLOUDY release, as well as for useful discussions. ARA thanks CNPq for financial support. RFP acknowledges financial support from the European Union's Horizon 2020 research and innovation program under the Marie Skłodowska-Curie grant agreement No. 721463 to the SUNDIAL ITN network. AV acknowledges support from grant AYA2016-77237-C3-1-P from the Spanish Ministry of Economy and Competitiveness (MINECO).

REFERENCES

- Ahn C. P. et al., 2014, *ApJS*, 211, 17
- Alton P. D., Smith R. J., Lucey J. R., 2018, *MNRAS*, 478, 4464
- Baldwin C., McDermid R. M., Kuntschner H., Maraston C., Conroy C., 2018, *MNRAS*, 473, 4698
- Balzano V. A., 1983, *ApJ*, 268, 602
- Bica E., 1988, *A&A*, 195, 76
- Bica E., Alloin D., 1987, *A&A*, 186, 49
- Boggs P. T., Rogers J. E., 1990, in Brown P. J., Fuller W. A., eds, *Proc. Conf. Vol 112, AMS-IMS-SIAM Joint Summer Research, Contemporary Mathematics: Statistical Analysis of Measurement Error Models and Applications*. Anerucab Natgenatucak Sicut, Rhode Island, p. 186
- Borguet B. C. J., Edmonds D., Arav N., Benn C., Chamberlain C., 2012, *ApJ*, 758, 69
- Burtscher L. et al., 2015, *A&A*, 578, A47
- Cardelli J. A., Clayton G. C., Mathis J. S., 1989, *ApJ*, 345, 245
- Cenarro A. J., Cardiel N., Gorgas J., Peletier R. F., Vazdekis A., Prada F., 2001, *MNRAS*, 326, 959
- Cesetti M. et al., 2009, *A&A*, 497, 41
- Chen Y.-P., Trager S. C., Peletier R. F., Lançon A., Vazdekis A., Prugniel P., Silva D. R., Gonneau A., 2014, *A&A*, 565, A117
- Chies-Santos A. L., Larsen S. S., Wehner E. M., Kuntschner H., Strader J., Brodie J. P., 2011a, *A&A*, 525, A19
- Chies-Santos A. L., Larsen S. S., Kuntschner H., Anders P., Wehner E. M., Strader J., Brodie J. P., Santos J. F. C., 2011b, *A&A*, 525, A20
- Condon J. J., Cotton W. D., Broderick J. J., 2002, *AJ*, 124, 675
- Conroy C., van Dokkum P. G., 2012, *ApJ*, 760, 71
- Cushing M. C., Vacca W. D., Rayner J. T., 2004, *PASP*, 116, 362
- Dahmer-Hahn L. G. et al., 2019, *MNRAS*, 482, 5211
- Dahmer-Hahn L. G., Riffel R., Rodríguez-Ardila A., Martins L. P., Kehrig C., Heckman T. M., Pastoriza M. G., Dametto N. Z., 2018, *MNRAS*, 476, 4459
- Dametto N. Z. et al., 2019, *MNRAS*, 482, 4437
- Dametto N. Z., Riffel R., Pastoriza M. G., Rodríguez-Ardila A., Hernandez-Jimenez J. A., Carvalho E. A., 2014, *MNRAS*, 443, 1754
- Ferguson J. W., Korista K. T., Baldwin J. A., Ferland G. J., 1997, *ApJ*, 487, 122
- Ferland G. J. et al., 2017, *Rev. Mex. Astron. Astrofis.*, 53, 385
- Ferruit P., Wilson A. S., Mulchaey J., 2000, *ApJS*, 128, 139
- Filho M. E., Fraternali F., Markoff S., Nagar N. M., Barthel P. D., Ho L. C., Yuan F., 2004, *A&A*, 418, 429
- Francois P., Morelli L., Pizzella A., Ivanov V. D., Coccato L., Cesetti M., Corsini E. M., Dalla Bonta E., 2019, *A&A*, 621, A60
- Frogel J. A., Stephens A., Ramírez S., DePoy D. L., 2001, *AJ*, 122, 1896
- Genzel R., Tacconi L. J., Rigopoulou D., Lutz D., Tecza M., 2001, *ApJ*, 563, 527
- Girardi L., Bressan A., Bertelli G., Chiosi C., 2000, *A&AS*, 141, 371
- Goddard D. et al., 2017, *MNRAS*, 465, 688
- González Delgado R. M. et al., 2015, *A&A*, 581, A103
- Gonçalves A. C., Veron P., Veron-Cetty M.-P., 1998, *A&AS*, 127, 107
- Hamann F., 1998, *ApJ*, 500, 798
- Hamann F. W., Barlow T. A., Chaffee F. C., Foltz C. B., Weymann R. J., 2001, *ApJ*, 550, 142
- Ho L. C., Filippenko A. V., Sargent W. L. W., 1997a, *ApJS*, 112, 315
- Ho L. C., Filippenko A. V., Sargent W. L. W., Peng C. Y., 1997b, *ApJS*, 112, 391
- Hummer D. G., Storey P. J., 1987, *MNRAS*, 224, 801
- Kotilainen J. K., Hyvönen T., Reunanen J., Ivanov V. D., 2012, *MNRAS*, 425, 1057
- La Barbera F., Ferreras I., Vazdekis A., de la Rosa I. G., de Carvalho R. R., Trevisan M., Falcón-Barroso J., Ricciardelli E., 2013, *MNRAS*, 433, 3017
- Lamperti I. et al., 2017, *MNRAS*, 467, 540
- Lançon A., Goldader J. D., Leitherer C., González Delgado R. M., 2001, *ApJ*, 552, 150
- Lyubenova M., Kuntschner H., Rejkuba M., Silva D. R., Kissler-Patig M., Tacconi-Garman L. E., Larsen S. S., 2010, *A&A*, 510, A19
- Maraston C., 1998, *MNRAS*, 300, 872
- Maraston C., 2005, *MNRAS*, 362, 799
- Maraston C., Strömbäck G., 2011, *MNRAS*, 418, 2785
- Marigo P., Girardi L., Bressan A., Groenewegen M. A. T., Silva L., Granato G. L., 2008, *A&A*, 482, 883
- Mármol-Queraltó E. et al., 2009, *ApJ*, 705, L199
- Martín-Navarro I., Vazdekis A., Falcón-Barroso J., La Barbera F., Yıldırım A., van de Ven G., 2018, *MNRAS*, 475, 3700
- Martins L. P., Rodríguez-Ardila A., Diniz S., Gruenewald R., de Souza R., 2013a, *MNRAS*, 431, 1823
- Martins L. P., Rodríguez-Ardila A., Diniz S., Riffel R., de Souza R., 2013b, *MNRAS*, 435, 2861
- Mason R. E. et al., 2015, *ApJS*, 217, 13
- McDermid R. M. et al., 2015, *MNRAS*, 448, 3484
- Noël N. E. D., Greggio L., Renzini A., Carollo C. M., Maraston C., 2013, *ApJ*, 772, 58
- Oliva E. et al., 2001, *A&A*, 369, L5
- Origlia L., Moorwood A. F. M., Oliva E., 1993, *A&A*, 280, 536
- Origlia L., Ferraro F. R., Fusi Pecci F., Oliva E., 1997, *A&A*, 321, 859
- Pereira-Santaella M., Diamond-Stanic A. M., Alonso-Herrero A., Rieke G. H., 2010, *ApJ*, 725, 2270
- Pogge R. W., Owen J., 1993, Ohio State University, Internal Report, 9301, p. 1
- Rayner J. T., Toomey D. W., Onaka P. M., Denault A. J., Stahlberger W. E., Vacca W. D., Cushing M. C., Wang S., 2003, *PASP*, 115, 362
- Rieke G. H., Lebofsky M. J., Thompson R. I., Low F. J., Tokunaga A. T., 1980, *ApJ*, 238, 24
- Riffel R. et al., 2015, *MNRAS*, 450, 3069
- Riffel R., Borges Vale T., 2011, *Ap&SS*, 334, 351
- Riffel R., Rodríguez-Ardila A., Pastoriza M. G., 2006, *A&A*, 457, 61

Riffel R., Pastoriza M. G., Rodríguez-Ardila A., Maraston C., 2007, *ApJ*, 659, L103

Riffel R., Pastoriza M. G., Rodríguez-Ardila A., Maraston C., 2008, *MNRAS*, 388, 803

Riffel R., Pastoriza M. G., Rodríguez-Ardila A., Bonatto C., 2009, *MNRAS*, 400, 273

Riffel R., Ruschel-Dutra D., Pastoriza M. G., Rodríguez-Ardila A., Santos J. F. C. Jr, Bonatto C. J., Ducati J. R., 2011a, *MNRAS*, 410, 2714

Riffel R., Bonatto C., Cid Fernandes R., Pastoriza M. G., Balbinot E., 2011b, *MNRAS*, 411, 1897

Riffel R., Riffel R. A., Ferrari F., Storchi-Bergmann T., 2011c, *MNRAS*, 416, 493

Riffel R., Rodríguez-Ardila A., Aleman I., Brotherton M. S., Pastoriza M. G., Bonatto C., Dors O. L., 2013b, *MNRAS*, 430, 2002

Riffel R. A. et al., 2013a, *MNRAS*, 429, 2587

Röck B., 2015, PhD thesis, Instituto de Astrofísica de Canarias

Röck B., Vazdekis A., Ricciardelli E., Peletier R. F., Knapen J. H., Falcón-Barroso J., 2016, *A&A*, 589, A73

Röck B., Vazdekis A., La Barbera F., Peletier R. F., Knapen J. H., Allende-Prieto C., Aguado D. S., 2017, *MNRAS*, 472, 361

Roek B., 2015, PhD thesis, Instituto de Astrofísica de Canarias

Salaris M., Weiss A., Cassarà L. P., Piován L., Chiosi C., 2014, *A&A*, 565, A9

Sánchez-Blázquez P., Gorgas J., Cardiel N., González J. J., 2006, *A&A*, 457, 787

Sánchez S. F. et al., 2016, *A&A*, 594, A36

Sanders D. B., Mirabel I. F., 1996, *ARA&A*, 34, 749

Sanders D. B., Mazzarella J. M., Kim D.-C., Surace J. A., Soifer B. T., 2003, *AJ*, 126, 1607

Schmitt H. R., Calzetti D., Armus L., Giavalisco M., Heckman T. M., Kennicutt R. C. Jr, Leitherer C., Meurer G. R., 2006, *ApJ*, 643, 173

Silva D. R., Kuntschner H., Lyubenova M., 2008, *ApJ*, 674, 194

Sturm E. et al., 2006, *ApJ*, 653, L13

Tayal S. S., 2004, *ApJS*, 150, 465

Thomas D., Maraston C., Bender R., 2003, *MNRAS*, 339, 897

Trager S. C., Faber S. M., Worthey G., González J. J., 2000, *AJ*, 119, 1645

Vacca W. D., Cushing M. C., Rayner J. T., 2003, *PASP*, 115, 389

van Dokkum P. G., Conroy C., 2012, *ApJ*, 760, 70

Vazdekis A., Ricciardelli E., Cenarro A. J., Rivero-González J. G., Díaz-García L. A., Falcón-Barroso J., 2012, *MNRAS*, 424, 157

Vazdekis A., Koleva M., Ricciardelli E., Röck B., Falcón-Barroso J., 2016, *MNRAS*, 463, 3409

Veilleux S., 2006, *New Astron. Rev.*, 50, 701

Veilleux S., Kim D.-C., Sanders D. B., Mazzarella J. M., Soifer B. T., 1995, *ApJS*, 98, 171

Villaume A., Conroy C., Johnson B., Rayner J., Mann A. W., van Dokkum P., 2017, *ApJS*, 230, 23

Wang J. L., Xia X. Y., Mao S., Cao C., Wu H., Deng Z. G., 2006, *ApJ*, 649, 722

Worthey G., Faber S. M., Gonzalez J. J., 1992, *ApJ*, 398, 69

Worthey G., Faber S. M., Gonzalez J. J., Burstein D., 1994, *ApJS*, 94, 687

Zibetti S., Gallazzi A., Charlot S., Pierini D., Pasquali A., 2013, *MNRAS*, 428, 1479

SUPPORTING INFORMATION

Supplementary data are available at *MNRAS* online.

Appendix A. Final Reduced Spectra.

Appendix B. Literature Data.

Please note: Oxford University Press is not responsible for the content or functionality of any supporting materials supplied by the authors. Any queries (other than missing material) should be directed to the corresponding author for the article.

APPENDIX A: FINAL REDUCED SPECTRA

Final reduced and redshift-corrected spectra for the remaining sample. Available as online material.

APPENDIX B: LITERATURE DATA

Here we present the measurements using the index definitions listed in Table 5 for the literature data. The data used here are those of Dahmer-Hahn et al. (2018) and Baldwin et al. (2017). For the latter we found optical Sloan Digital Sky Survey data (Ahn et al. 2014) for four sources. For the remaining objects we collected the values of Fe5015, Mg_b, and Fe5270 from McDermid et al. (2015), while for the sources of Dahmer-Hahn et al. (2018) the optical data were taken from the Calar Alto Legacy Integral Field Area Survey (CALIFA Sánchez et al. 2016) and we measured the EW of the optical lines.

Table B1. Absorption feature EWs (in Å) from the sample of Baldwin et al. (2017). The full table is available as online material.

Line	IC0719	NGC 3032	NGC 3098	NGC 3156	NGC 3182	NGC 3301
Ca4227	1.68 ± 0.01	–	–	0.56 ± 0.00	1.41 ± 0.00	–
G4300	6.23 ± 0.04	–	–	1.94 ± 0.00	5.57 ± 0.01	–
Fe4383	5.99 ± 0.05	–	–	1.89 ± 0.00	5.33 ± 0.01	–
Ca4455	2.07 ± 0.02	–	–	1.08 ± 0.00	1.68 ± 0.00	–
Fe4531	3.67 ± 0.04	–	–	2.99 ± 0.00	3.37 ± 0.01	–

Note. The values of Fe5015, Mg_b, and Fe5270 for NGC 3032, NGC 3098, and NGC 3301 were taken from McDermid et al. (2015) for Re/8.

Table B2. Absorption feature EWs (in Å) from the sample of Baldwin et al. (2017). The full table is available as online material.

Line	NGC 3489	NGC 4379	NGC 4578	NGC 4608	NGC 4710	NGC 5475
Ca4227	–	–	–	–	–	1.32 ± 0.00
G4300	–	–	–	–	–	5.76 ± 0.01
Fe4383	–	–	–	–	–	5.43 ± 0.01
Ca4455	–	–	–	–	–	1.87 ± 0.00
Fe4531	–	–	–	–	–	3.79 ± 0.01

Table B3. Absorption feature EWs (in Å) from the sample of Dahmer-Hahn et al. (2018). The full table is available as online material.

Line	N4636	N5905	N5966	N6081	N6146	N6338	UGC08234
Ca4227	–	–	1.23 ± 0.10	1.21 ± 0.07	1.00 ± 0.03	1.16 ± 0.06	0.76 ± 0.05
G4300	–	–	5.54 ± 0.28	5.59 ± 0.30	5.30 ± 0.16	5.82 ± 0.23	3.01 ± 0.21
Fe4383	–	–	4.46 ± 0.35	4.56 ± 0.29	4.47 ± 0.24	4.33 ± 0.29	2.63 ± 0.25
Ca4455	–	–	1.36 ± 0.16	1.14 ± 0.15	1.04 ± 0.13	1.30 ± 0.17	0.92 ± 0.15
Fe4531	–	–	3.32 ± 0.14	3.04 ± 0.21	3.15 ± 0.14	3.24 ± 0.12	2.73 ± 0.08

Note. The optical data were taken from CALIFA survey (Sánchez et al. 2016). N means NGC.

This paper has been typeset from a \LaTeX file prepared by the author.